Hrubišák, F., Hušeková, K., Zheng, X., Rosová, A., Dobročka, E., Ťapajna, M., Mičušík, M., Nádaždy, P., Egyenes, F., Keshtkar, J., Kováčová, E., Pomeroy, J. W., Kuball, M., & Gucmann, F. (2023). Heteroepitaxial growth of Ga_2O_3 on 4H-SiC by liquid-injection MOCVD for improved thermal management of Ga_2O_3 power devices. *Journal of Vacuum Science and Technology A: Vacuum, Surfaces and Films*, *41*(4), [042708]. https://doi.org/10.1116/6.0002649

Peer reviewed version

Link to published version (if available):
10.1116/6.0002649

Journal of Vacuum Science & Technology A

Heteroepitaxial growth of Ga_2O_3 on 4H-SiC by liquid-injection MOCVD for improved thermal management of Ga_2O_3 power devices

Running title: Heteroepitaxial growth of Ga_2O_3 on 4H-SiC by LI-MOCVD

Running Authors: Hrubišák et al.

Fedor Hrubišák[1], Kristína Hušeková[1], Xiang Zheng[2,a)], Alica Rosová[1], Edmund Dobročka[1], Milan Ťapajna[1], Matej Mičušík[3], Peter Nádaždy[1], Fridrich Egyenes[1], Javad Keshtkar[1], Eva Kováčová[1], James W. Pomeroy[2], Martin Kuball[2], and Filip Gucmann[1,4,a)]

[1]Institute of Electrical Engineering, Slovak Academy of Sciences, Dúbravská cesta 9, 841 04 Bratislava, Slovakia
[2]Center for Device Thermography and Reliability, HH Wills Physics Laboratory, University of Bristol, Tyndall Avenue, Bristol, BS8 1TL, United Kingdom
[3]Polymer institute, Slovak Academy of Sciences, Dúbravská cesta 9, 845 41 Bratislava, Slovakia
[4]Centre for Advanced Materials Application SAS, Dúbravská cesta 9, Bratislava 845 11, Slovakia

[a)] Electronic mail: filip.gucmann@savba.sk, xiang.zheng@bristol.ac.uk (thermal analysis)

We report on the growth of monoclinic β- and orthorhombic κ-phase Ga_2O_3 thin films using liquid-injection metal-organic chemical vapor deposition (LI-MOCVD) on highly thermally conductive 4H-SiC substrates using Gallium (III) acetylacetonate or tris(2,2,6,6-tetramethyl-3,5-heptanedionato) gallium (III). Both gallium precursors produced the β phase, while only use of the latter led to growth of κ-Ga_2O_3. Regardless of the used precursor, best results for β-Ga_2O_3 were achieved at growth temperature of 700 °C and O_2 flows in the range 600 – 800 sccm. A relatively narrow growth window was found for κ-Ga_2O_3 and best results were achieved for growth temperatures of 600 °C and O_2 flow of 800 sccm. While phase-pure β-Ga_2O_3 was prepared, κ-Ga_2O_3 showed various degree of parasitic β phase inclusions.

X-ray diffraction and transmission electron microscopy confirmed highly textured structure of β- and κ-Ga_2O_3 layers resulting from the presence of multiple in-plane domain orientations.

Thermal conductivities of 53 nm-thick β-Ga_2O_3 (2.13 +0.29/-0.51 W/m-K) and 45 nm-thick κ-Ga_2O_3 (1.23 +0.22/-0.26 W/m-K) were determined by transient thermoreflectance and implications for device applications were assessed.

Presented results suggest great potential of heterointegration of Ga_2O_3 and SiC for improved thermal management and reliability of future Ga_2O_3-based high power devices.

I. INTRODUCTION

Ultra-wide bandgap (UWBG) semiconductors represent very promising electronic materials for next generation of power electronics, greatly extending capabilities of currently used wide bandgap (WBG) semiconductors such as GaN and SiC. Competitive material properties, controlled n-type doping, and available native substrates resulted in recent increased research focus in Ga_2O_3, even surpassing that of other typical UWBG materials, i.e. AlN, AlGaN, or diamond. High expectations of UWBG Ga_2O_3 over WBG GaN and SiC stem from favorable comparison of well-established figures of merit (FOMs). These allow to benchmark device limits when a particular material is used for device applications. Typical FOMs used in power electronics are e.g. Johnson's FOM (JFOM = $E_{br}^2 \cdot v_{sat}^2/4\cdot\pi^2$), Baliga's FOM (BFOM = $\varepsilon\cdot\mu\cdot E_{br}^3$) and Huang's material FOM (HMFOM = $E_{br}\cdot\sqrt{\mu}$), where E_{br} represents material's breakdown electric field (Ga_2O_3: >8 MV·cm^{-1}, GaN: 3.5 MV·cm^{-1}, SiC: 2.0 – 2.5 MV·cm^{-1})[1–3], v_{sat} is electron saturation velocity (Ga_2O_3: 2.0×10^7 cm·s^{-1}, GaN, SiC: 2.0 – 2.5×10^7 cm·s^{-1})[1,2,4,5], ε is dielectric constant, and μ is the

mobility of charge carriers. JFOM predicts semiconductor radio-frequency (RF) capabilities (Ga_2O_3: 2844, GaN: 1089, SiC: 278)[4,6] while BFOM predicts semiconductor power-switching capability (Ga_2O_3: 3214, GaN: 846, SiC: 317)[4,7]. HMFOM reflects suitability for high-frequency power switching applications (Ga_2O_3: 12, GaN: 10, SiC = 7)[8,9]. Even though inferior in case of expected achievable electron mobility[10] and similar saturation velocity, Ga_2O_3 offers almost 2.5 – 3× higher breakdown field compared to GaN and SiC secures its potentially strong position in the field of power electronics.

Apart from high breakdown electric field and high carrier saturation velocity at high voltages, high power densities, or high switching frequencies, thermal conductivity of the base device material play an important role in keeping the on-state device temperature within the reasonable limits for reliable long-term operation[11]. Unfortunately, low and anisotropic lattice thermal conductivity represents one of the key issues in Ga_2O_3 device technology. Compared to WBG GaN (170 W/m-K)[1] and SiC (~300 – 400 W/m-K)[2] or UWBG AlN (~260 – 370 W/m-K)[12,13] and diamond (~2000 W/m-K)[14–16], bulk thermal conductivity of Ga_2O_3 is substantially lower[17]; e.g. α-Ga_2O_3: ~10 W/m-K, β-Ga_2O_3: from ~9 W/m-K in [100] direction to ~27 W/m-K in [010] direction, κ-Ga_2O_3: ~11 W/m-K.

Six Ga_2O_3 crystal phases with slight differences in their material properties were identified: α (rhombohedral), β (monoclinic), γ (cubic – defective spinel), δ (cubic – bixbyite), ε (pseudo-hexagonal), and κ (orthorhombic)[3,18,19]. Monoclinic β-Ga_2O_3 is the only thermodynamically stable phase; the others are metastable and can typically convert to β-Ga_2O_3 at higher temperatures[3]. As a result, bulk growth of single crystal Ga_2O_3 was only demonstrated for monoclinic β phase; typical range of used methods include Czochralski, edge-defined film-fed growth (EFG), floating zone (FZ), or vertical Bridgman

Journal of Vacuum Science & Technology A

(VB)[10,20,21]. Epitaxial growth of thin films of all Ga_2O_3 phases is typically done using standard techniques[22], i.e. halide vapor-phase epitaxy (HVPE)[18,23–25], molecular-beam epitaxy (MBE)[26–30], atomic layer deposition (ALD)[31–33], pulsed-laser deposition (PLD)[34,35], and by variety of chemical vapor deposition (CVD) methods – metalorganic chemical vapor deposition (MOCVD)[32,36,37], mist-CVD[38–43], or liquid-injection MOCVD (LI-MOCVD)[44,45].

The LI-MOCVD growth technique used in this study represents a low-pressure variation of MOCVD where precursor is delivered in liquid form; powdered precursors are typically dissolved in a suitable organic solvent. The growth method is similar to low-pressure chemical vapor deposition (LP-CVD) previously studied by other groups[46–50]. The main difference is that LP-CVD utilizes solid gallium precursor, typically in a form of high purity Ga pellets[48] instead of Ga-based metalorganic. In case of LI-MOCVD, the liquid nature of precursor solution offers great versatility in used chemical sources compared to other CVD techniques. Another key difference is the temperature range used for growth of Ga_2O_3. LP-CVD growth of Ga_2O_3 is typically achieved at temperatures > 800 °C[46,47,51] and shows high growth rates of ~1 – 10 μm/h[46]. The LI-MOCVD technique uses lower growth temperature in the range of ~550 – 700 °C which allows for successful synthesis of metastable α- and κ-Ga_2O_3 polymorphs besides the thermodynamically stable monoclinic β-Ga_2O_3 produced by LP-CVD, however at much lower growth rates[46,48].

Homoepitaxial growth on native β-Ga_2O_3 substrates was shown on various substrate orientations, e.g. (010), (001), (100), $(\bar{2}01)$[52,53]. Heteroepitaxy of Ga_2O_3 targeted MgO[54,55] as a foreign substrate material in several studies, however, an intense research effort was devoted predominantly to the use of affordable sapphire of various orientations

to achieve high quality films[43,56,57]. Use of silicon substrates usually led to amorphous or polycrystalline Ga_2O_3 layers[58–60]; single crystalline β-Ga_2O_3 on Si was demonstrated using the catalyst-modified vapor-liquid-solid method (VLS), however the thickness of resulting layers was only ~15 nm[61].

While a clear advancement in the field of Ga_2O_3 heteroepitaxy was achieved, it is expected, that heterointegration of Ga_2O_3 with high thermal conductivity materials such as SiC, AlN, or diamond will be necessary for achieving high power outputs of Ga_2O_3 devices, as maintaining their on-state device temperature at the acceptable levels resulting in improved device reliability and lifetime[62,63]. In fact, there was an increased recent effort in heterointegration of Ga_2O_3 and SiC, AlN, and diamond using either wafer bonding[64–66] or thin film growth techniques[29,42,67–71]. In this work, we focus on the heteroepitaxial growth of β- and κ-Ga_2O_3 thin films on 4H-SiC substrates for improved thermal management of Ga_2O_3 power devices using a low-pressure liquid-injection MOCVD method. Detailed analysis of structural and thermal properties of prepared Ga_2O_3 layers is presented and discussed.

II. EXPERIMENTAL DETAILS

Monoclinic β- and orthorhombic κ-Ga_2O_3 thin films were grown on Si-terminated highly-resistive 4H-SiC substrates using custom-built low-pressure liquid-injection metalorganic chemical vapor deposition (LI-MOCVD) system with horizontal hot-wall quartz reactor. Schematics of used deposition system and prepared samples are shown in Fig. 1. More information on this method can be found elsewhere[44]. Gallium (III) acetylacetonate ($Ga(acac)_3$) or tris(2,2,6,6-tetramethyl-3,5-heptanedionato) gallium (III)

($Ga(thd)_3$) dissolved in toluene (0.02 mol/l) were used as Ga precursors and as a liquid solution injected into the evaporation part of the LI-MOCVD unit kept at 180 °C using electronically-controlled electromagnetic injection microvalve. O_2 and Ar were used as reaction and carrier gases, respectively. Silicon tetraethyl orthosilicate (TEOS) was used to achieve n-type doping in all prepared samples; 0.1 mol % TEOS concentration in the precursor solution was used. Growth parameters are summarized in Tab. 1. Number of injections was 5000 and thickness of grown layers was evaluated by ellipsometry or X-ray reflectivity (XRR).

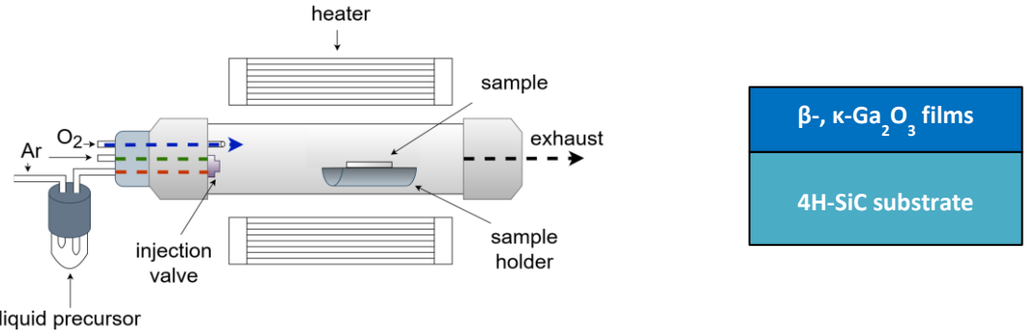

FIG. 1. Schematics of used LI-MOCVD setup used for Ga_2O_3 growth and prepared thin films.

TABLE I. Summary of used Ga_2O_3 growth parameters.

Sample	Ga_2O_3 phase	Precursor	Growth temperature (°C)	O_2/Ar flow (sccm)	Pressure (Torr)	Growth rate (nm/h)	Thickness (nm)
A	β	$Ga(acac)_3$	700	600/120	1.68	63	88
B	β	$Ga(thd)_3$	700	600/120	1.68	40	55
C	κ	$Ga(thd)_3$	600	800/120	2.06	27	35

Room temperature (RT) van der Pauw measurement was used to evaluate resistivity (ρ) of prepared Ga_2O_3 layers. Ohmic contacts for this measurement were manufactured

using 60 nm Ti / 100 nm Au e-beam-evaporated metallic stack followed by alloying using rapid thermal annealing (RTA) in forming gas (FGA, 10 % H_2, 90 % N_2) atmosphere at 550 °C for 30 min. When no doping was used, all Ga_2O_3 layers regardless of the grown phase were highly resistive ($\rho>10^5$ Ω·cm). Si-doped β-Ga_2O_3 layers showed resistivity of ~1.6 Ω·cm, while Si-doped κ-Ga_2O_3 remained highly resistive.

X-ray photoelectron spectroscopy (XPS) was employed to provide depth elemental composition profiling. XPS signals were recorded using a Thermo Scientific K-Alpha XPS system equipped with a micro-focused, monochromatic Al Ka X-ray source (1486.68 eV). An X-ray beam (6 mA×12 kV) of 400 μm size was used. The spectra were acquired in the constant analyzer energy mode with pass energy of 200 eV for the survey. Narrow regions were collected using the pass energy of 50 eV. Charge compensation was achieved with the system flood gun. Depth profile analysis was done using ion gun (1.4 μA of 3 keV Ar^+ ions over 14 mm^2) sputtering. The Thermo Scientific Avantage software 5.9931 was used for digital data acquisition and processing. Spectral calibration was determined by automated calibration routine and the internal Au, Ag, and Cu standards. The surface composition in atomic % was determined from the integrated peak areas of the detected atoms (I_A) and the respective sensitivity factors (s_A).

X-ray diffraction (XRD) was used to evaluate the prepared Ga_2O_3 layers. Bruker D8 DISCOVER diffractometer equipped with X-ray source with rotating Cu anode operating at 12 kW was used. XRD measurements were performed in parallel beam geometry with parabolic Goebel mirror in the primary beam; resulting beam divergence was ~0.03°. Beam size of 1 × 6 mm^2 was used for acquisition of symmetrical ω /2θ scans. During the measurements the samples were tilted by an angle of 0.5° away from the precise

SiC 0004 diffraction position to suppress the strong diffracted intensity from the substrate. φ scans of the selected Ga_2O_3 and SiC diffractions were acquired to evaluate the azimuthal ordering of the layer structure. To decrease the effect of defocusing, the beam size for these measurements was reduced to 1×2 mm^2 and parallel-plate collimator with the angular acceptance 0.35° was inserted into the diffracted beam.

To analyze the surface and the microstructure of Ga_2O_3 layers, scanning electron microscope (SEM) FEI Quanta in secondary electrons detection mode and transmission electron microscope (TEM) JEOL JEM-1200EX were used, respectively. Thin plan-view specimens were prepared by a combination of conventional mechanical lapping an Ar^+ ion-beam thinning from the substrate side of selected samples using liquid nitrogen-cooled (LN) sample holder; the cross-sectional TEM specimens were prepared using focused ion beam (FIB) technique.

Thermal characterization was performed using a pump-probe-based transient thermoreflectance (TTR) on β- and κ-Ga_2O_3 layers; full details of the technique can be found elsewhere[72,73]. To achieve sufficient sensitivity to Ga_2O_3 thermal properties, specific samples targeting Ga_2O_3 thicknesses close to 50 nm were prepared. In case of β-Ga_2O_3 (thickness ~53 nm), only sample grown using $Ga(acac)_3$ precursor was evaluated. κ-Ga_2O_3 sample (thickness ~45 nm) was prepared using $Ga(thd)_3$ precursor. These Ga_2O_3 samples were coated with 100 nm Au on a 10-nm thick Ti adhesion layer as a heat transducer. A 532 nm continuous wave laser was used to monitor the surface reflectivity while a 355 nm pulsed laser periodically heated the surface (Au transducer). The monitored change in the reflectivity is linearly proportional to the temperature on the surface. The thermal properties of different layers of the sample were then extracted from the TTR signal. A

three layer 2-D heat diffusion model of β-Ga_2O_3 or κ-Ga_2O_3, i.e. transducer/Ga_2O_3/SiC, was used to fit the measured TTR traces[72]. Three different locations were measured on each sample to confirm they produce similar TTR trace. At each measured location, measurements were repeated three times and then averaged to increase the signal to noise ratio. Monte Carlo analysis was performed (500 times) to provide a distribution of the target values to the fitted parameters.

Surface morphology and root-mean-square (RMS) surface roughness was evaluated by atomic force microscopy (AFM) using NT-MDT NTEGRA Prima in tapping mode. Optical bandgap determination of the prepared Ga_2O_3 layers using optical transmittance/absorption method was attempted, however could not be resolved due to the strong absorption in the SiC substrate.

III. RESULTS AND DISCUSSION

A. Structure and surface morphology

1. X-ray photoelectron spectroscopy

Ga_2O_3 stoichiometry and growth-related carbon content was investigated using XPS on sample A (β phase). XPS survey spectrum was recorded from the surface of sample A. Only signals related to C, O, and Ga were observed (Fig. 2 (a)). Detailed scans including C, O, and Ga signals (Fig. S1 in supplementary material) were recorded from the surface of sample A and from the volume of the grown Ga_2O_3 films after 12 s of etching by in-situ Ar^+ ion sputtering to remove surface contamination. Ga and O signals were attributed to Ga_2O_3. Assuming most intense signals – Ga 3d at ~21 eV (Fig. S1 (a)) and O 1s at ~531 eV (Fig. S1 (b)), predominantly stoichiometric Ga_2O_3 was concluded (Tab. S1). Weak Ga

3d signal at ~19 eV (Fig. S1 (a)) and weak O 1s signal at ~533 eV (Fig. S1 (b)) correspond to a negligible Ga-suboxide content which may be related to disordered Ga_2O_3 grain boundaries.

Surface C-related signal likely corresponded to adventitious carbon contamination and decreased below the instrument detection limit (<0.1 at %) after surface etching (Fig. 2 (b)). Low C-related signal suggest C content in Ga_2O_3 was within reasonable limits and did not cause detrimental Ga_2O_3 lattice alteration (see XRD results in the following section). Since used LI-MOCVD growth method uses relatively low pressure (~0.1 – 1 Torr), carbon incorporation in Ga_2O_3 layers may be significant as was observed in e.g. MOCVD-grown GaN[74]. However, this seems unlikely in our case; we expect the majority of carbon produced from used solvents and organometallics after their thermal decomposition did not incorporate into the Ga_2O_3 layer and left the LI-MOCVD unit, possibly reacting with the gaseous oxygen. We note, that, while not resolved by XPS, the amount of carbon in grown Ga_2O_3 may be still sufficient to significantly contribute to various charge trapping phenomena and needs to be further evaluated.

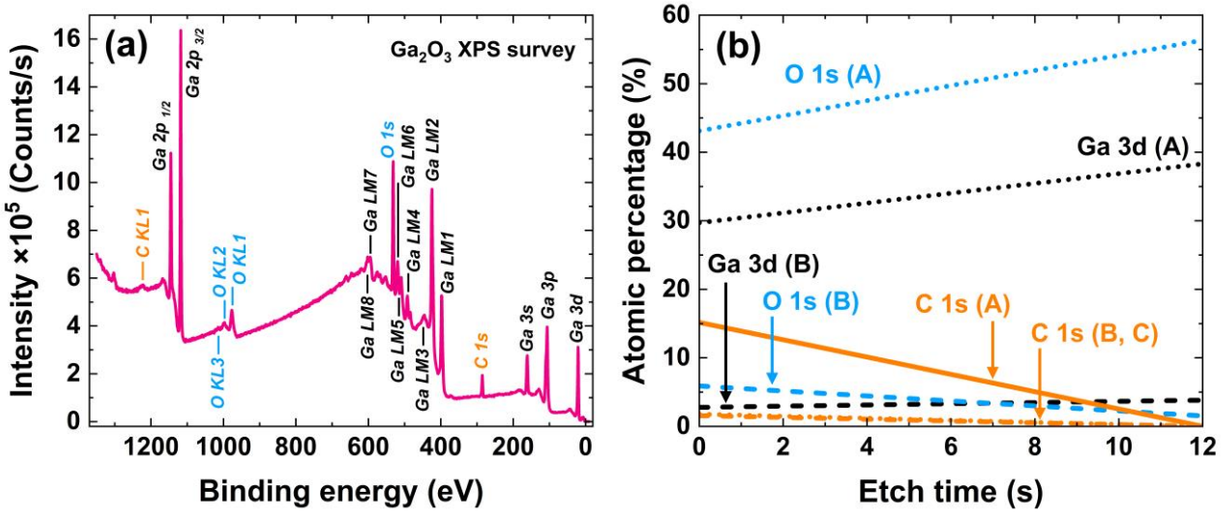

FIG. 2. XPS results for β-Ga_2O_3 (sample A). Surface XPS survey spectrum; only Ga, O, and C signals were observed (a) and calculated depth-resolved atomic percentages of Ga, O, and C after Ar^+ ion sputtering (b). Etch time at 0 s corresponds to the sample surface.

2. *X-ray diffraction*

XRD confirmed single-phase $(\bar{2}01)$ β-Ga_2O_3 in samples A and B grown using $Ga(acac)_3$ and $Ga(thd)_3$, respectively. In case of samples A and B, only reflections of $(\bar{2}01)$ Ga_2O_3 lattice planes, i.e. $\bar{2}01$, $\bar{4}02$, and $\bar{6}03$ diffractions were observed. As reported elsewhere, phase identification of orthorhombic κ-Ga_2O_3 using only XRD can provide inconclusive results.[45] However, as discussed later, using a combination of XRD and TEM we conclude single-phase κ-Ga_2O_3 with a minor inclusion of β-Ga_2O_3 in sample C grown using $Ga(thd)_3$. Corresponding wide symmetric ω/2θ XRD scans are shown in Fig. 3, rocking curves (ω scans) are shown in Fig. S2. Approximately 2-fold larger full width at half maximum (FWHM) of corresponding rocking curves for sample grown using $Ga(acac)_3$ than those grown using $Ga(thd)_3$ precursors was observed, indicating improved crystal quality of the latter, likely related to lower observed growth rates when the $Ga(thd)_3$ was used (c.f. Tab. 1). This behavior is consistent with our previous findings for β-Ga_2O_3 grown on sapphire substrates [44]. Similar to previous reports on sapphire substrates[44,57,75,76], six in-plane domain orientations were observed in our samples as confirmed by XRD φ scans shown in Fig. 4 (a-b). Due to negligible difference between samples A and B, only φ scans of the former are shown in Fig. 4 (a). We note, that in sample C, both major orthorhombic κ phase and minor parasitic β phase showed this behavior.

Based on our XRD results, LI-MOCVD growth of monoclinic β-Ga_2O_3 on 4H-SiC at 700 °C using $Ga(acac)_3$ precursor was in general less sensitive to O_2 flows used. O_2 flows >600 sccm led to repeatable phase-pure synthesis. However, when $Ga(thd)_3$ was used, a mixture of β and κ phases was often observed. Best results in repeatable growth of phase-pure β-Ga_2O_3 was achieved at similar conditions to those observed when $Ga(acac)_3$ precursor was used, i.e. 700 °C growth temperature and O_2 flow >600 sccm.

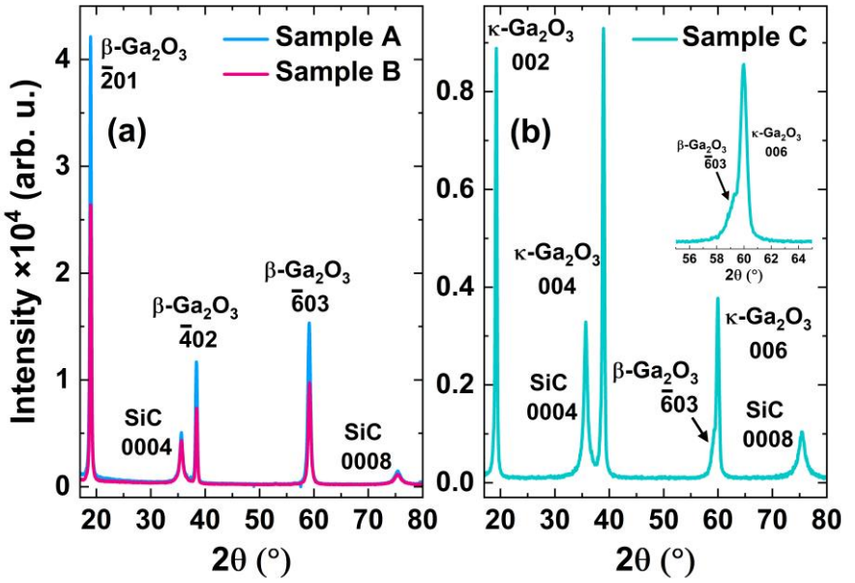

FIG. 3. Symmetric ω/2θ XRD scans of sample A and B – β-Ga_2O_3 (a) and sample C – κ-Ga_2O_3 (b). Inset in (b) shows detail of the 006 κ-Ga_2O_3-related diffraction with a shoulder attributed to $\bar{6}03$ diffraction of the parasitic β-Ga_2O_3.

Growth of orthorhombic κ-Ga_2O_3 was observed only when a $Ga(thd)_3$ precursor was used. For all investigated κ-Ga_2O_3 growth conditions, some degree of parasitic β phase inclusion was observed. Fig. 5 illustrates the contribution of parasitic β-Ga_2O_3 phase in LI-MOCVD-grown κ-Ga_2O_3 films as a function of growth temperature (560 – 700 °C) and O_2

flow (200 – 800 sccm). Using measured ω/2θ XRD scans, diffractions at 2θ angles close to 60 °, i.e. at the locations corresponding to respective $\bar{6}03$ and 006 diffractions of β- and κ-Ga_2O_3, were approximated by Gaussian peak fitting and κ/β-Ga_2O_3 peak height ratio was plotted. The most significant suppression of parasitic β-Ga_2O_3 phase was observed at growth temperature of 600 °C and O_2 flow of 800 sccm. In this regard, varying the growth temperature and O_2 flow showed relatively narrow κ-Ga_2O_3 growth window, i.e. growth temperature ~600 – 630 °C and O_2 flow ~700 – 800 sccm. We expect the parasitic β-Ga_2O_3 may be further suppressed when higher O_2 flows are used, however 800 sccm represented the achievable limit for the used LI-MOCVD setup. A combination of lowest used growth temperature and O_2 flow resulted in unsuccessful Ga_2O_3 growth.

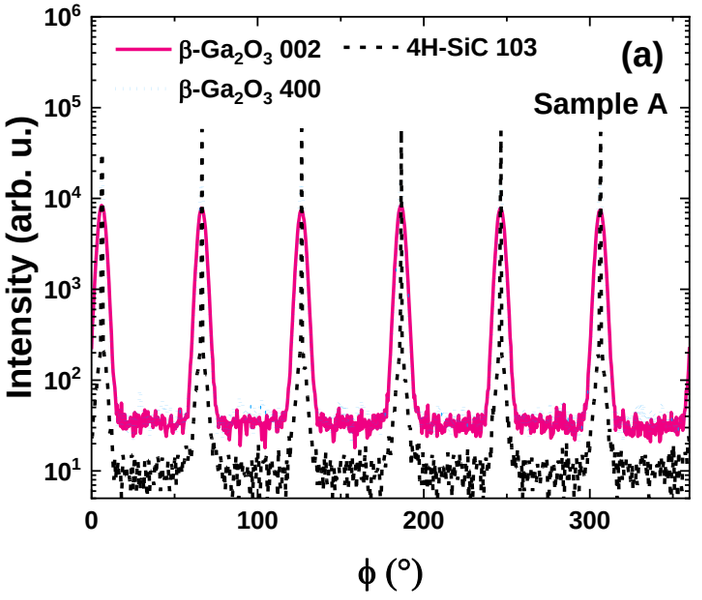

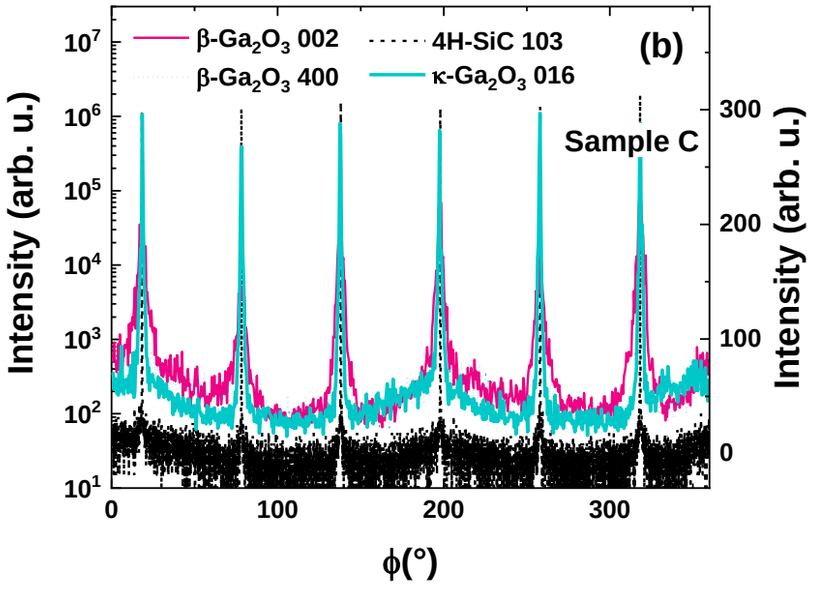

FIG. 4. XRD φ scans of prepared β- and κ-Ga_2O_3 films. Sample A showing six maxima related to 002 and 400 diffractions of β-Ga_2O_3 and related 103 diffraction of 4H-SiC substrate (a). Sample C showing six maxima related to 016 diffraction of κ-Ga_2O_3, 002 and 400 diffractions of parasitic β-Ga_2O_3 contribution (right intensity scale), and 103 diffraction of 4H-SiC substrate (left intensity scale) (b).

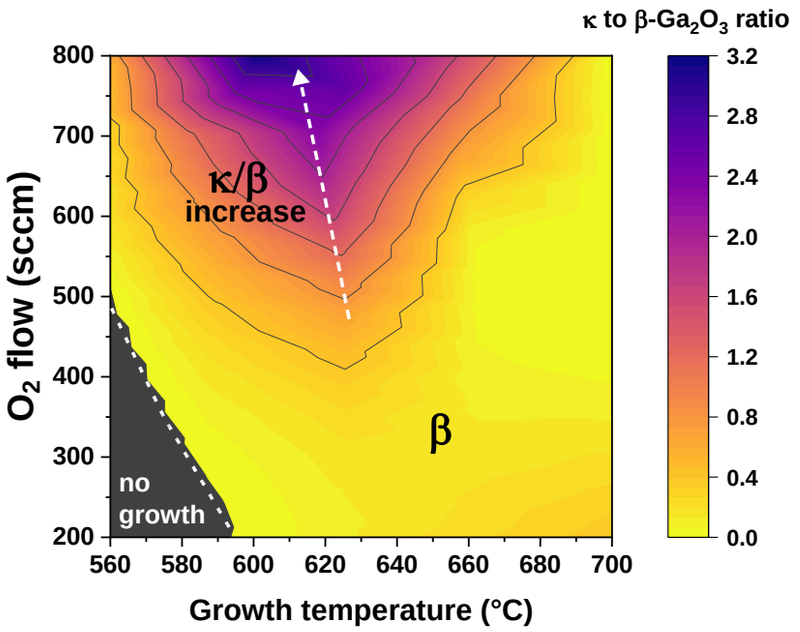

FIG. 5. A map showing the influence of growth temperature and O_2 flow on the inclusion of parasitic β-Ga_2O_3 phase in κ-Ga_2O_3 films grown by LI-MOCVD on 4H-SiC. Z-scale represents the ratio of κ to β peak heights determined by Gaussian fitting of ω/2θ XRD diffractions at the locations of $\bar{6}03$ and 006 diffractions of β and κ-Ga_2O_3, respectively.

3. *Electron microscopy*

A growth of relatively large faceted grains is characteristic for β-Ga_2O_3 layers (Fig. 6 (a)); the faceting is slightly more pronounced for the thicker sample A grown using $Ga(acac)_3$ than for the sample B grown using $Ga(thd)_3$. Electron diffraction from plane-view TEM specimen of sample A (Fig. 6) confirmed the epitaxial relation observed using XRD, i.e. $(\bar{2}01)[102]$ β-Ga_2O_3 || $(0001)[01\bar{1}0]$ 4H-SiC as well as the presence of six in-plane domain orientations. Assuming this epitaxial relationship, Fig. 6 (b) schematically depicts the possible orientations of β-Ga_2O_3 (red, yellow, and green rectangles) on SiC

substrate (black triangles). Only three β-Ga_2O_3 orientations (rectangles) are depicted in the growth schematic. Due to the low symmetry of monoclinic β-phase, shown rectangles do not represent the identical orientations after two-fold rotation, i.e. each rectangle in fact represents two different domain orientations.

The long diffraction arcs observed in Fig. 6 (d) reflect misorientations of diffracting planes in Ga_2O_3 domains. These however do not directly express the misorientation of domain lattices because the observed electron diffraction pattern with seemingly six-fold rotation symmetry is in fact composed of many electron diffraction patterns originated in individual domains, which do not have the six-fold symmetry. The ideal angle between $(\bar{2}01)$ and (512) planes is 91.66° and between (512) and (020) planes is 61.72°. Thus, the origin of the widening of diffraction arcs observed in SAED and also in the XRD β-phase φ-scan maxima (Fig. 4a) can be attributed to a combination of real domain misorientation and low symmetry of monoclinic phase which consequently results in non-symmetric diffraction patterns.

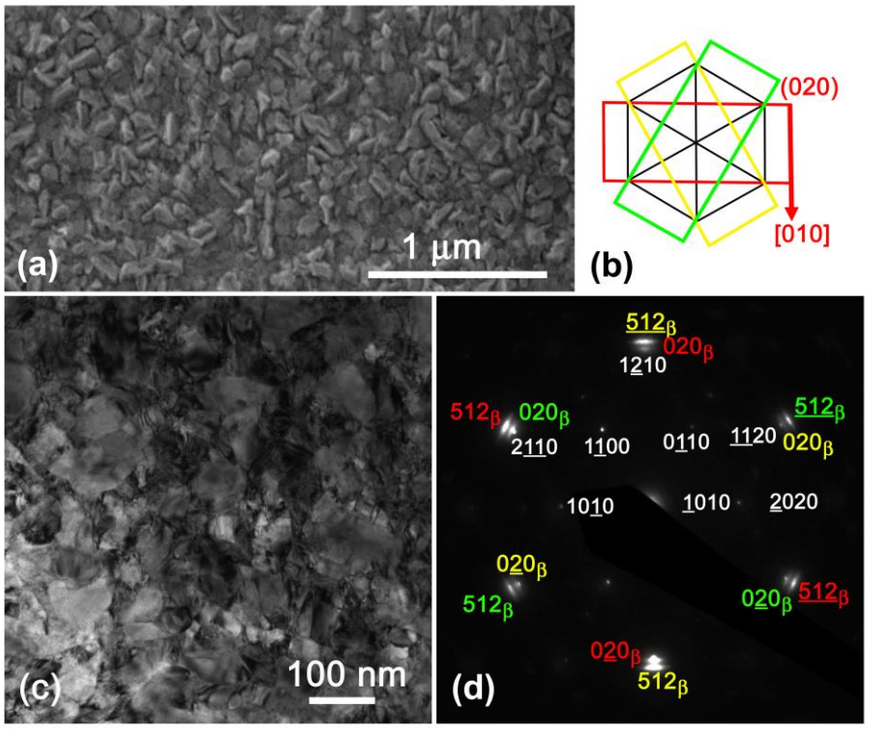

FIG. 6. SEM image of the surface of sample A (a). Schematic representation of epitaxial relation between the β-Ga_2O_3 layer (red, yellow, and green rectangles) and 4H-SiC substrate (black triangles) (b). TEM plan view of sample A (c) and corresponding indexed SAED pattern (d). The white indices correspond to the SiC substrate and colored ones correspond to different domain orientations of β-Ga_2O_3. Colors used correspond to those used the schematic showed in (b).

The sample C (κ-Ga_2O_3) showed much smoother sufrace and the Ga_2O_3 layer consisted of considerably smaller domains (Fig. 7 (a)) compared to sample A. All TEM observations confirmed the epitaxial relation (001)[010] κ-Ga_2O_3 // (0001)[01$\bar{1}$0] 4H-SiC. The bright field (BF) TEM image (Fig. 7 (a)) was taken with the specimen oriented precisely with SiC [0001] zone axis parallel to the electron beam, thus the observed Moiré patterns created by double diffraction reveal mutual in-plane and out-of plane

misorientations of individual domains. In the SAED pattern shown in Fig 7 (b), the strongest principial diffractions are indexed preferentially, while the indexing of weak intensity diffractions is illustrated by the green indicies belonging to only one domain orientation. All weak diffractions corresponding to every domain orientation together with additional spots related to double diffractions create rather complex diffraction pattern (Fig. 7b)). These weak diffraction spots in all orientation domains confirm the presence of κ-phase in our layers as they cannot be attributed to hexagonal ε-Ga_2O_3 phase[45]. The schematic in Fig 7 (c) illustrates the mutual orientation of six different domain orientations and their relationship to the 4H-SiC substrate. Only three rectangles are shown in the schematic as the κ-phase symmetry group $Pna2_1$ does not contain two-fold rotation axis parallel to [001] direction. The XRD analysis revealed the presence of a minor epitaxially grown β-phase. Its occurance is also visible in the plan-view SAED pattern and illustrated in a magnified detail shown in Fig. 7 (d) as the arc-shaped weak diffraction spots located between 1210 SiC and 330 and 060 family of κ-phase diffractions (labeled by green arrow in Fig. 7 (d)). Due to clarity, the β-phase diffraction spots are not indexed in the Figures 7 (b) and (d), however, they are the same as those in Fig. 6 (d) which can be used as a reference. Green arrow in Fig. 7 (d) denotes the 020 family diffraction spots; 512 β-phase diffraction spots are superposed to the 060 and 330 family spots belonging to κ-phase. Because of their location, it is not possible to distinguish the β-Ga_2O_3 domain distribution in the layer using conventional dark field (DF) image technique. The weak arc spots labeled by the red arrows in Fig. 7 (d) were created by double diffraction.

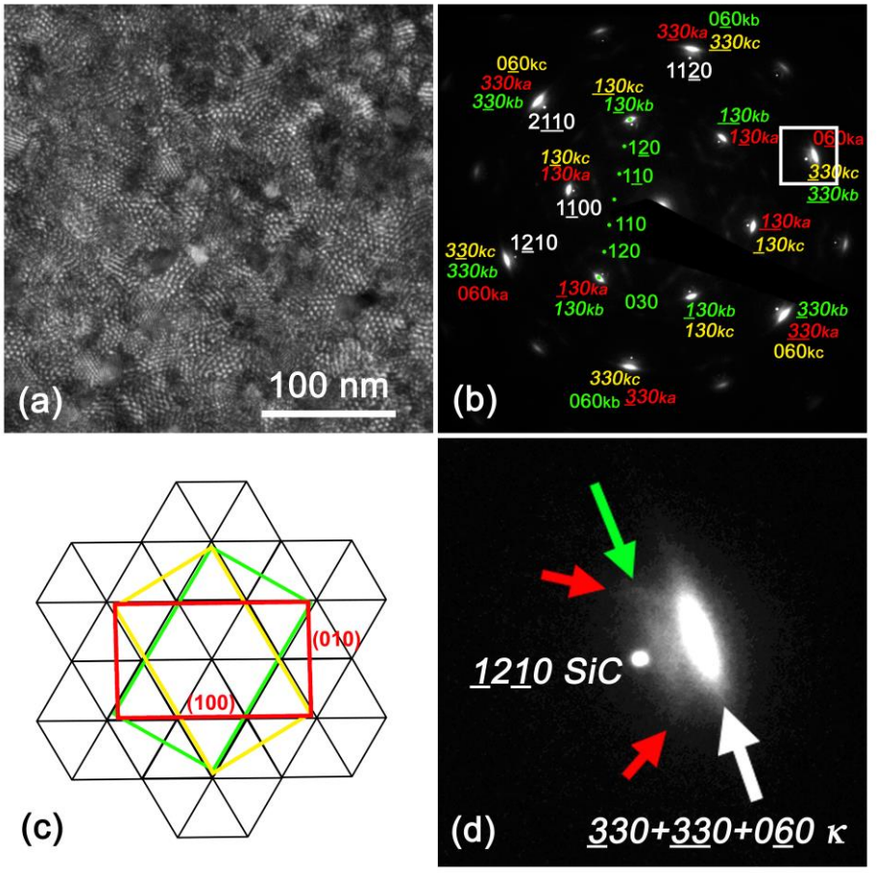

FIG. 7. TEM plan view of sample C (a) with corresponding SAED pattern (b). Schematic representation of epitaxial relation between the κ-Ga_2O_3 domain orientations (red, yellow, and green rectangles) and 4H-SiC substrate (black triangles) (c). Detail SAED pattern corresponding to the area in (b) denoted by white rectangle (d).

Similary to the plan-view TEM analysis, sample C cross-sectional electron diffraction patterns can be indexed according to the orthorhombic κ-phase Ga_2O_3 (Fig. 8(c)).

As can be seen in the cross-sectional TEM images in Fig. 8 (a) and (b), the κ-phase Ga_2O_3 in the sample C layer exhibited colmunar growth of thin domains, following the initial growth of an intermediate layer of variable thickness. A detailed study on the structure of this intermediate layer, as well as its role in the growth of κ-phase Ga_2O_3 will be published

elsewhere. The thin κ-phase Ga_2O_3 domains were visualised by dark field technique using 013 diffraction (Fig. 8 (b)).

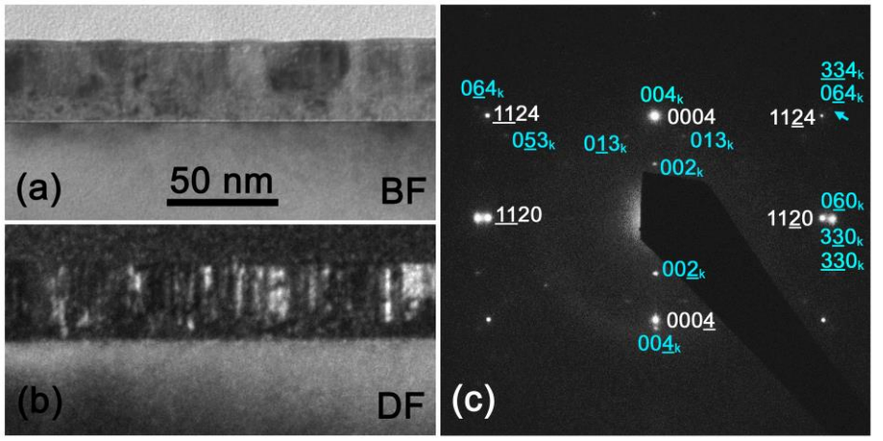

FIG. 8. Cross-sectional TEM of κ-Ga_2O_3 (sample C). Bright field (a) and dark field TEM images (b) and corresponding SAED pattern (c). White indices in (c) correspond to 4H-SiC substrate and the cyan indices correspond to different κ-Ga_2O_3 domain orientations. The DF image in (b) was taken using 013 diffraction.

Observed domain structure hindering the crystal quality of κ-Ga_2O_3 layer in sample C is likely caused by the large lattice mismatch between Ga_2O_3 and 4H-SiC. For example, the mismatch along [100] κ-Ga_2O_3 and [$10\bar{1}0$] 4H-SiC is approximately 5.4% leading to a domain structure resulting from strain relaxation[77]. The single-domain κ-Ga_2O_3 growth was only achieved on an exotic ε-$GaFeO_3$ substrate[78] suggesting a suitable buffer layer may improve crystal properties of Ga_2O_3 on SiC. However, domain structure similar to our case was observed when AlN buffer was used for κ-Ga_2O_3 layers[78].

4. *Atomic force microscopy*

AFM confirmed the granular surface in all three studied samples (Fig. 9 (a-c)). β-Ga_2O_3 (samples A and B) showed similar respective RMS surface roughness of 6.5 and 6.8 nm. Sample A, grown using $Ga(acac)_3$ showed more uniform surface coverage than sample B grown using $Ga(thd)_3$. Despite of the same number of injections during the LI-MOCVD growth, the thickness of the sample B was ~60% smaller compared to sample A, i.e. a slower growth and/or longer nucleation phase could have resulted in the observed less uniform surface coverage and can possibly be mitigated by prolonged growth. Much lower surface roughness was observed for κ-Ga_2O_3, i.e. ~0.9 nm. Surface line profiles of samples A, B, and C positioned along the dashed lines displayed in corresponding AFM scans are also shown in Fig. 9.

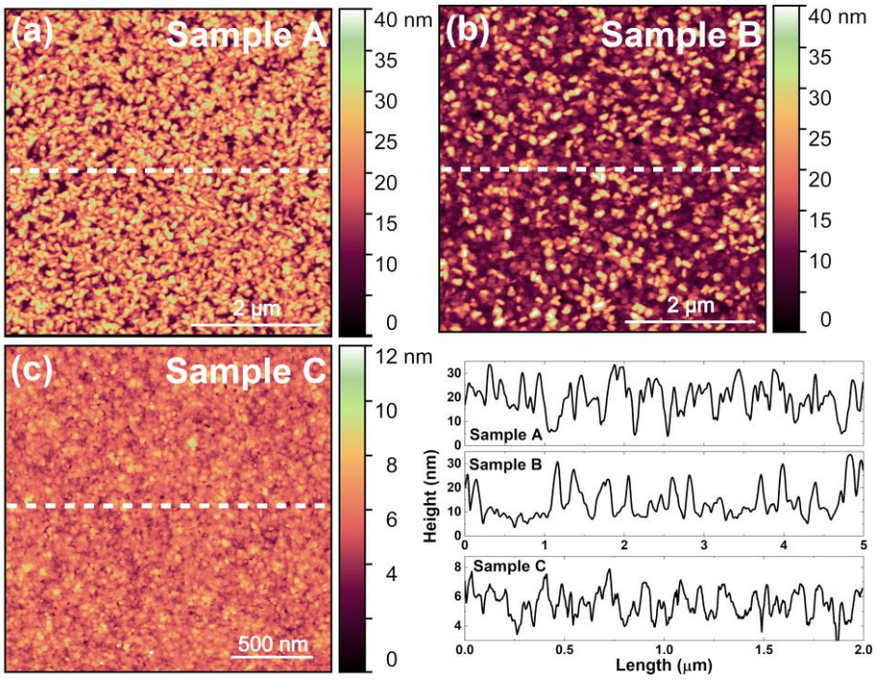

FIG. 9. AFM-resolved surface morphology. β-Ga_2O_3 grown using $Ga(acac)_3$ – sample A (a) and $Ga(thd)_3$ – sample B precursors. κ-Ga_2O_3 grown using $Ga(thd)_3$ precursor –

sample C. Also shown are corresponding line profiles taken along dashed lines. Following respective RMS surface roughness for samples A, B, and C were determined: 6.5 nm, 6.8 nm, and 0.9 nm.

Low surface roughness of κ-Ga_2O_3 (~0.9 nm) is a promising result which can enable e.g. κ-Ga_2O_3/III-N heterostructure growth, where low interfacial roughness is desirable. κ-Ga_2O_3 is expected to provide strong polarization charge[79] and forming heterostructures with III-N materials could enable Ga_2O_3 devices with 2D electron gas (2DEG) channel[80,81]. Thermal stability of this metastable polymorph will however play a crucial role in any kind of heterointegration attempts, limiting the growth of available barrier materials atop the κ-Ga_2O_3.

B. Thermal properties

Fig. 10 shows the measured TTR signals and best fitting results for the 3-layers model; thermal properties of the samples included Au, Ga_2O_3, and the 4H-SiC substrate. Literature values were used for density and heat capacity of all layers. Thermal conductivities of Ga_2O_3 and SiC were the fitting parameters. Thermal boundary resistance (TBR) of Au(Ti)/Ga_2O_3 and Ga_2O_3/SiC interfaces were lumped into the Ga_2O_3 layer. This is because the thermal conductivity of the Ga_2O_3 is comparable to that of the interlayer between the Ga_2O_3 and SiC when the thickness of the Ga_2O_3 is only at the tens of nanometer level[82]; this makes the TBR value challenging to distinguish. Nevertheless, lumping the TBR with the thermal conductivity of the Ga_2O_3 layer has only limited effect on the fitted resulting value of the Ga_2O_3 thermal conductivity as its thickness is much greater (5 – 6 ×) than that of the interface layer. Estimated transducer/Ga_2O_3 TBR was close

to e.g. Au/Si, indicating a negligible error on the fitting and determined resulting Ga_2O_3 thermal conductivity.

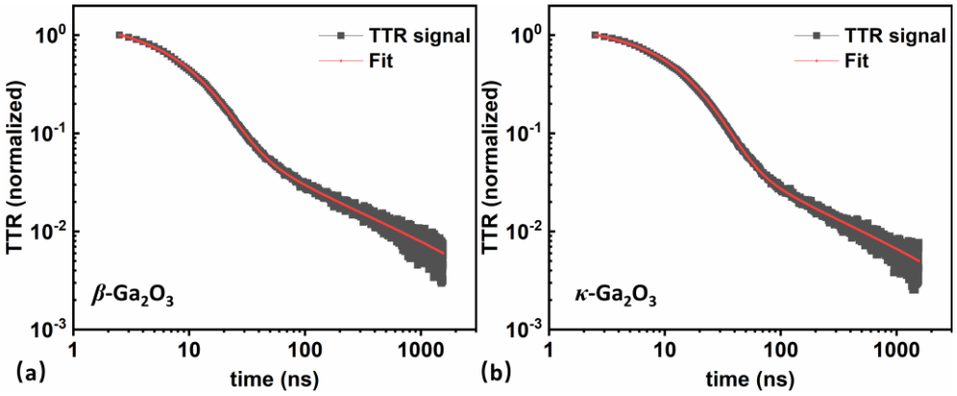

FIG. 10. TTR signals and 3-layers model fitting results for β-Ga_2O_3 (a) and κ-Ga_2O_3 (b).

Figure 11 shows a sensitivity analysis of the TTR signal to a 10% change in the thermal conductivity of Ga_2O_3 and TBR of Ti/Ga_2O_3 and Ga_2O_3/SiC interfaces. The sensitivity analysis demonstrates the effect of each parameter on the TTR signal. The sensitivity analysis shows distinct sensitivity time scales between the thermal conductivity of Ga_2O_3 and other layers, and other parameters including the heat capacity, allowing it to be accurately fitted. It is important to note that the out-of-plane thermal conductivity of β-Ga_2O_3 and κ-Ga_2O_3 is assumed dominant; the in-plane thermal conductivity is of low sensitivity in the model for such a thin Ga_2O_3 film. In case the TBR values (Au/Ga_2O_3 and/or Ga_2O_3/SiC) were assumed in the model, there would be large related uncertainty because their sensitivities in the sensitivity analysis would be much smaller than those of the Ga_2O_3. We note, that the surface roughness can affect the reflected TTR signal, which could represent a concern e.g. for the β-Ga_2O_3 sample (RMS surface roughness ~7 nm). However, owing to the high sensitivity to Ga_2O_3 layer as shown in the sensitivity analysis

(Fig. 11), sufficient TTR signal-to-noise ratio was obtained to achieve good fit to the experimental data (Fig.10).

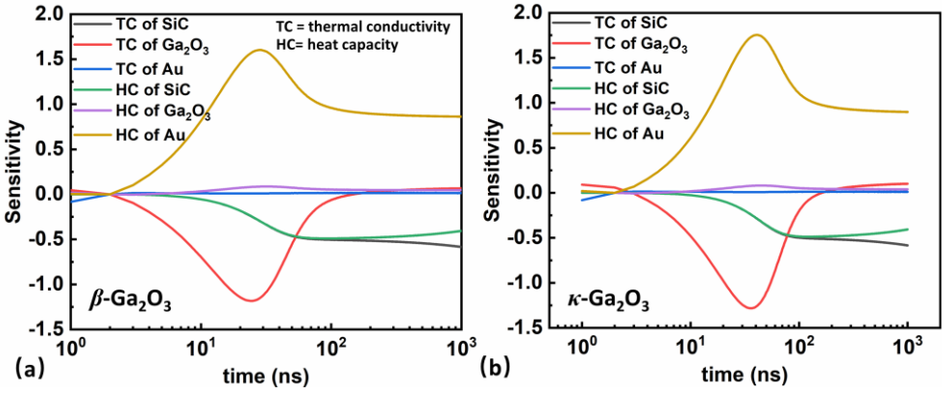

FIG. 11. TTR sensitivity analysis for β-Ga_2O_3 (a) and κ-Ga_2O_3 (b).

Monte Carlo (MC) error analysis was employed to estimate the error bar in the thermal conductivity of Ga_2O_3 by repeating the model fitting 500 times (Fig. S3). The initial values of fitting parameters of the sample and the laser were randomly varied within 5% standard deviation for each time. Thermal conductivities of the 53 nm-thick β-Ga_2O_3 and 45 nm-thick κ-Ga_2O_3, i.e. samples A and C, were 2.13 +0.29/-0.51 W/m-K and 1.23 +0.22/-0.26 W/m-K, respectively, consistent with the reported predictions for various Ga_2O_3 thickness[83].

C. *Impact on device thermal characteristics*

To assess the influence of the heterointegration of LI-MOCVD-grown Ga_2O_3 and highly thermally conductive SiC substrate on the channel temperature of Ga_2O_3-based transistors, thermal simulation of an example of metal-oxide-semiconductor field-effect transistor (MOSFET) was made. An Ansys finite element thermal simulation was used to

predict the temperature distribution in a β-Ga_2O_3/SiC MOSFET with various thicknesses of Ga_2O_3 layer. The peak channel temperatures were compared between devices on SiC and on Ga_2O_3 substrates. Thickness-dependent thin-film Ga_2O_3 thermal conductivity of 5, 12.9, 13.2, and 14 W/m-K at 300 K for 500 nm, 2 μm, 6.5 μm Ga_2O_3, and Ga_2O_3 substrate, respectively, based on our measurements and extrapolations[83] was used in the simulation. Temperature-dependent thermal conductivities of Ga_2O_3 layer and 4H-SiC substrates were adopted from previous studies[84,85]. The thickness of the gate metal and the Ohmic contacts was taken as 150 and 160 nm, respectively; thermal conductivity of gold was taken as 315 W/m-K. A 20 nm-thick Al_2O_3 layer was considered as the gate insulator. Gate-drain, gate-source, and gate lengths were taken as 6, 6, and 2 μm, respectively, same as previously reported in actual devices[86]. Heat generation in the transistor channel (length of 1.5 μm) was defined at the drain edge of the gate contact to a depth of 50 nm. Ambient temperature was 25 °C.

Fig. S4 shows a comparison for a homoepitaxial Ga_2O_3 device and the device integrated with SiC for various thicknesses of Ga_2O_3 device layer. The peak temperature was simulated for power densities ranging from 1 to 5 W/mm. The Ga_2O_3/SiC device thermal resistance of ~9.7 mm-K/W is much lower compared to ~190 mm-K/W for Ga_2O_3 homoepitaxy, when a thin Ga_2O_3 layer (<2 μm) is used, because the heat source is very close to SiC, resulting in efficient heat extraction. This means, thinner Ga_2O_3 layer can increase the ability of heat removal of the device even though thinner Ga_2O_3 layer results in a drop in its thermal conductivity. Device thermal resistance of ~9.7 mm-K/W for simulated Ga_2O_3/SiC MOSFET with thin Ga_2O_3 layer (<2 μm) is comparable to GaN/Si

high electron mobility transistor (HEMT, ~10 mm-K/W) and ~2× higher compared to GaN/SiC HEMT (~5 mm-K/W) when similar device layouts are considered[63,87].

Fig. 12 shows a comparison of device depth temperature profiles at the device center assuming various thicknesses of the Ga_2O_3 layer; Dissipated power density of 3W/mm was assumed. The 500 nm and 2 μm Ga_2O_3 layer has negligible effect on the total device thermal resistance, while the 6.5 μm Ga_2O_3 accounts for almost 4 times higher device thermal resistance. The homoepitaxial Ga_2O_3 device showed ~18 times higher total thermal resistance at 3 W/mm, compared to the structure with thin (<2 μm) Ga_2O_3 layer on SiC substrate.

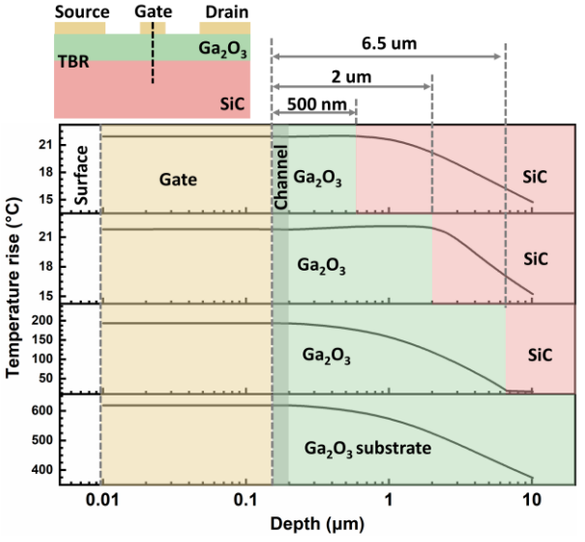

FIG. 12. Simulated device depth temperature profiles for various thicknesses of the Ga_2O_3 layer at 3 W/mm. Temperatures for homoepitaxial Ga_2O_3 device are shown for comparison.

The interlayer between the Ga_2O_3 and SiC substrate in the simulation was approximated by a layer with the thickness of 10 nm and a thermal conductivity of 2.1 W/m-K, the same value measured by the TTR for the 50 nm-thick β-Ga_2O_3 layer. The

thermal conductivity of the interlayer was fixed for different Ga_2O_3 layer thicknesses used in the simulation. Thermal simulation assuming 5× lower and higher thermal conductivity of this interlayer was also performed, however only <1% temperature difference was observed. This indicates that for the chosen device design and dissipated power density range, the thermal boundary resistance between the LI-MOCVD-grown Ga_2O_3 and 4H-SiC does not significantly contribute to the thermal performance of a real Ga_2O_3 device, regardless of the Ga_2O_3 thickness.

IV. SUMMARY AND CONCLUSIONS

A successful epitaxial growth of thin monoclinic β- and orthorhombic κ-Ga_2O_3 films on highly thermally conductive 4H-SiC substrates using LI-MOCVD was demonstrated. $Ga(acac)_3$ and $Ga(thd)_3$ were used as gallium precursors; β-Ga_2O_3 was prepared using both precursors, while only $Ga(thd)_3$ enabled the growth of κ-Ga_2O_3. Regardless of the used precursor, best results for β-Ga_2O_3 were achieved at growth temperature of 700 °C and O_2 flows in range 600 – 800 sccm. In contrast, based on the used growth conditions, κ-Ga_2O_3 showed various degree of parasitic β phase inclusion. Relatively narrow growth window for κ-Ga_2O_3 was identified and best results were achieved for growth temperature of 600 °C and O_2 flow of 800 sccm. Complete suppression of parasitic β phase may be achieved for O_2 flows >800 sccm. Undoped Ga_2O_3 layers were highly resistive regardless of their phase ($\rho>10^5$ Ω·cm); Si-doped β-Ga_2O_3 layers showed low resistivity of ~1.7 Ω·cm, while Si-doped κ-Ga_2O_3 layers remained highly resistive. Complex domain orientation structures of grown β- and κ-Ga_2O_3 films was revealed by the

XRD and TEM analyses. Stoichiometric Ga_2O_3 films were confirmed by XPS; minor Ga-suboxide content was attributed to disordered grain boundaries. Despite relatively low growth pressure, negligible growth-related C contamination (<0.1 at. %) was observed.

Transient thermoreflectance was used to determine the thermal conductivities of 53 nm-thick β-Ga_2O_3 and 45 nm-thick κ-Ga_2O_3 layers, i.e., 2.13 +0.29/-0.51 W/m-K and 1.23 +0.22/-0.26 W/m-K, respectively, in good agreement with previous reports. Computer thermal simulations of an example β-Ga_2O_3/SiC MOSFET device with various Ga_2O_3 layer thickness (0.5 – 6.5 μm) were prepared; results for dissipated power density in the range of 1 – 5 W/mm were compared to homoepitaxial device. Thin (<2 μm) Ga_2O_3 layers have negligible contribution to the total device thermal resistance, which was found to be ~9.7 mm-K/W, comparable to GaN on Si technology and about twice as much as typical values for GaN/SiC HEMTs. Devices with 6.5 μm Ga_2O_3 showed almost 4 times higher thermal resistance and homoepitaxial device showed approximately 18 times higher thermal resistance at 3 W/mm compared to devices with 2 μm or less thick Ga_2O_3 layer on 4H-SiC substrate. This suggests that using a thinner Ga_2O_3 layer is more important for reducing the device thermal resistance than its thermal conductivity, even though it is lower for thinner Ga_2O_3 layers. Thermal boundary resistance between Ga_2O_3 and SiC was found to have negligible impact on the simulated device temperature. Approximating the Ga_2O_3/SiC TBR with the TTR-determined thermal conductivity of ~50 nm-thick β-Ga_2O_3 layer (2.1 W/m-K) and varying this value in the range from 5 times lower (0.42 W/m-K) to 5 times higher (10.5 W/m-K) produced <1% difference in the simulated device temperatures. Therefore, we can conclude, that for the investigated conditions, TBR between the LI-MOCVD-grown Ga_2O_3 and 4H-SiC does not

significantly contribute to the thermal performance of Ga_2O_3 MOSFET, regardless of the Ga_2O_3 thickness.

Our results show great potential of heterointegration of Ga_2O_3 and SiC for improved thermal management and reliability of future Ga_2O_3-based high power devices. While other substrate materials may offer other advantageous properties such as reduced cost (Si) or even higher thermal conductivity (diamond), relatively low lattice mismatch between β-Ga_2O_3 and 4H-SiC (~1.3 % with monoclinic (010) plane) makes SiC preferable to Si (~20.8 %) and diamond (~14.8 %)[29] for growth of thicker Ga_2O_3 films. To take full advantage of the outstanding Ga_2O_3 material properties, high crystal quality layers will be needed. As a next step in the Ga_2O_3/SiC epitaxy, we expect vicinal SiC substrates may bring considerable improvement.

SUPPLEMENTAL MATERIAL

See supplementary material at [URL will be inserted by AIP Publishing] for detailed XPS spectra, XRD rocking curves, TTR Monte Carlo analysis, and simulated peak device channel temperatures.

ACKNOWLEDGMENTS

We acknowledge the funding from Slovak Research and Development Agency (Grant Nos. APVV-20-0220 and SK-CN-21-0013), from Slovak Grant Agency VEGA (Grant No. 2/0100/21), and from Slovak Academy of Sciences Dokto Grant No. APP0424. This work was performed during the implementation of the project Building-up Centre for advanced materials application of the Slovak Academy of Sciences, ITMS project code 313021T081 supported by Research & Innovation Operational Programme funded by the

ERDF. MK was supported by the Royal Academy of Engineering through the Chair in Emerging Technologies Scheme. The thermal characterization was supported as part of the ULTRA, an Energy Frontier Research Center funded by the U.S. Department of Energy, Office of Science, Basic Energy Sciences at the University of Bristol under award DE-SC0021230.

AUTHOR DECLARATIONS

Conflicts of Interest

The authors have no conflicts to disclose.

Author Contributions

Fedor Hrubišák: Conceptualization (equal), Funding acquisition (equal), Investigation (equal), Methodology (equal), Visualization (equal), Writing - original draft (equal), Writing - review & editing (equal). **Kristína Hušeková**: Investigation (equal), Methodology (equal), Resources (equal), Writing - review & editing (equal). **Xiang Zheng**: Data curation (equal), Formal analysis (equal), Investigation (equal), Methodology (equal), Visualization (equal), Writing - review & editing (equal). **Alica Rosová**: Formal analysis (equal), Investigation (equal), Methodology (equal), Visualization (equal), Writing - review & editing (equal). **Edmund Dobročka**: Formal analysis (equal), Investigation (equal), Methodology (equal), Writing - review & editing (equal). **Milan Ťapajna**: Conceptualization (equal), Funding acquisition (equal), Supervision (equal), Validation (equal), Writing - review & editing (equal). **Matej Mičušík**: Formal analysis (equal), Investigation (equal), Methodology (equal), Writing - review & editing (equal). **Peter Nádaždy**: Investigation (equal), Methodology (equal),

Writing - review & editing (equal). **Fridrich Egyenes**: Investigation (equal), Methodology (equal), Writing - review & editing (equal). **Javad Keshtkar**: Investigation (equal), Methodology (equal), Writing - review & editing (equal). **Eva Kováčová**: Investigation (supporting). **James Pomeroy**: Methodology (equal), Writing - review & editing (equal). **Martin Kuball**: Funding acquisition (equal), Resources (equal), Supervision (equal), Writing - review & editing (equal). **Filip Gucmann**: Conceptualization (equal), Funding acquisition (equal), Investigation (equal), Project administration (equal), Writing - original draft (equal), Writing - review & editing (equal).

DATA AVAILABILITY

The data that supports the findings of this study are available within the article [and its supplementary material].

REFERENCES

[1] S.C. Bera, *Microwave High Power High Efficiency GaN Amplifiers for Communication* (Springer Nature Singapore, Singapore, 2022).
[2] C. Langpoklakpam, A.-C. Liu, K.-H. Chu, L.-H. Hsu, W.-C. Lee, S.-C. Chen, C.-W. Sun, M.-H. Shih, K.-Y. Lee, and H.-C. Kuo, "Review of Silicon Carbide Processing for Power MOSFET," Crystals (Basel) **12**(2), 245 (2022).
[3] M. Higashiwaki, *Gallium Oxide* (Springer International Publishing, Cham, 2020).
[4] M.A. Mastro, A. Kuramata, J. Calkins, J. Kim, F. Ren, and S.J. Pearton, "Perspective—Opportunities and Future Directions for Ga_2O_3," ECS J Solid State Sc **6**(5), P356–P359 (2017).
[5] R. Singh, T.R. Lenka, D.K. Panda, R.T. Velpula, B. Jain, H.Q.T. Bui, and H.P.T. Nguyen, "The dawn of Ga2O3 HEMTs for high power electronics - A review," Mat Sci Semicon Proc **119**, 105216 (2020).
[6] E. Johnson, "Physical limitations on frequency and power parameters of transistors," 1958 IRE International Convention Record, New York, NY, USA, 1965, pp. 27-34, doi: 10.1109/IRECON.1965.1147520.
[7] B.J. Baliga, "Power Semiconductor Device Figure of Merit for High-Frequency Applications," IEEE Electr Device L **10**(10), 455–457 (1989).

[8] A.Q. Huang, "New Unipolar Switching Power Device Figures of Merit," IEEE Electr Device L **25**(5), 298–301 (2004).
[9] G. Jessen, K. Chabak, A. Green, J. McCandless, S. Tetlak, K. Leedy, R. Fitch, S. Mou, E. Heller, S. Badescu, A. Crespo, and N. Moser, in *2017 75th Annual Device Research Conference (DRC)* (IEEE, 2017), pp. 1–2.
[10] E. Ahmadi, and Y. Oshima, "Materials issues and devices of α- and β-Ga_2O_3," J Appl Phys **126**(16), 160901 (2019).
[11] P.J. Wellmann, "Power Electronic Semiconductor Materials for Automotive and Energy Saving Applications – SiC, GaN, Ga_2O_3 , and Diamond," Z Anorg Allg Chem **643**(21), 1312–1322 (2017).
[12] Z. Cheng, Y.R. Koh, A. Mamun, J. Shi, T. Bai, K. Huynh, L. Yates, Z. Liu, R. Li, E. Lee, M.E. Liao, Y. Wang, H.M. Yu, M. Kushimoto, T. Luo, M.S. Goorsky, P.E. Hopkins, H. Amano, A. Khan, and S. Graham, "Experimental observation of high intrinsic thermal conductivity of AlN," Phys Rev Mater **4**(4), 044602 (2020).
[13] R. Yu, G. Liu, G. Wang, C. Chen, M. Xu, H. Zhou, T. Wang, J. Yu, G. Zhao, and L. Zhang, "Ultrawide-bandgap semiconductor AlN crystals: growth and applications," J Mater Chem C **9**(6), 1852–1873 (2021).
[14] S. Kidalov, and F. Shakhov, "Thermal Conductivity of Diamond Composites," Materials **2**(4), 2467–2495 (2009).
[15] J. Anaya, S. Rossi, M. Alomari, E. Kohn, L. Tóth, B. Pécz, and M. Kuball, "Thermal conductivity of ultrathin nano-crystalline diamond films determined by Raman thermography assisted by silicon nanowires," Appl Phys Lett **106**(22), (2015).
[16] R.B. Simon, J. Anaya, F. Faili, R. Balmer, G.T. Williams, D.J. Twitchen, and D.M. Kuball, "Effect of grain size of polycrystalline diamond on its heat spreading properties," Appl Phys Express **9**(6), (2016).
[17] M. Higashiwaki, "β-Ga_2O_3 material properties, growth technologies, and devices: a review," AAPPS Bulletin **32**(1), 3 (2022).
[18] Y. Li, X. Xiu, W. Xu, L. Zhang, H. Zhao, Z. Xie, T. Tao, P. Chen, B. Liu, R. Zhang, and Y. Zheng, "Pure-phase κ-Ga_2O_3 layers grown on c-plane sapphire by halide vapor phase epitaxy," Superlattice Microst **152**, 106845 (2021).
[19] I. Cora, F. Mezzadri, F. Boschi, M. Bosi, M. Čaplovičová, G. Calestani, I. Dódony, B. Pécz, and R. Fornari, "The real structure of ε-Ga_2O_3 and its relation to κ-phase," CrystEngComm **19**(11), 1509–1516 (2017).
[20] Z. Galazka, "Growth of bulk β-Ga_2O_3 single crystals by the Czochralski method," J Appl Phys **131**(3), 031103 (2022).
[21] H.F. Mohamed, C. Xia, Q. Sai, H. Cui, M. Pan, and H. Qi, "Growth and fundamentals of bulk *β*-Ga_2O_3 single crystals," J Semicond **40**(1), 011801 (2019).
[22] B.R. Tak, S. Kumar, A.K. Kapoor, D. Wang, X. Li, H. Sun, and R. Singh, "Recent advances in the growth of gallium oxide thin films employing various growth techniques—a review," J Phys D Appl Phys **54**(45), 453002 (2021).
[23] Y. Yao, S. Okur, L.A.M. Lyle, G.S. Tompa, T. Salagaj, N. Sbrockey, R.F. Davis, and L.M. Porter, "Growth and characterization of α-, β-, and ε-phases of Ga_2O_3 using MOCVD and HVPE techniques," Mater Res Lett **6**(5), 268–275 (2018).
[24] Y. Oshima, E.G. Víllora, and K. Shimamura, "Halide vapor phase epitaxy of twin-free α-Ga_2O_3 on sapphire (0001) substrates," Appl Phys Express **8**(5), 055501 (2015).

[25] Y. Oshima, E.G. Víllora, and K. Shimamura, "Quasi-heteroepitaxial growth of β-Ga_2O_3 on off-angled sapphire (0 0 0 1) substrates by halide vapor phase epitaxy," J Cryst Growth **410**, 53–58 (2015).
[26] M. Kracht, A. Karg, M. Feneberg, J. Bläsing, J. Schörmann, R. Goldhahn, and M. Eickhoff, "Anisotropic Optical Properties of Metastable (01 1 2) α-Ga_2O_3 Grown by Plasma-Assisted Molecular Beam Epitaxy," Phys Rev Appl **10**(2), 1 (2018).
[27] T. Oshima, T. Okuno, and S. Fujita, "Ga_2O_3 Thin Film Growth on *c* -Plane Sapphire Substrates by Molecular Beam Epitaxy for Deep-Ultraviolet Photodetectors," Jpn J Appl Phys **46**(11), 7217–7220 (2007).
[28] M. Holland, C.R. Stanley, W. Reid, R.J.W. Hill, D. a. J. Moran, I. Thayne, G.W. Paterson, and a. R. Long, "Ga_2O_3 grown on GaAs by molecular beam epitaxy for metal oxide semiconductor field effect transistors," J Vac Sci Technol B **25**(5), 1706 (2007).
[29] N. Nepal, D.S. Katzer, B.P. Downey, V.D. Wheeler, L.O. Nyakiti, D.F. Storm, M.T. Hardy, J.A. Freitas, E.N. Jin, D. Vaca, L. Yates, S. Graham, S. Kumar, and D.J. Meyer, "Heteroepitaxial growth of β-Ga_2O_3 films on SiC via molecular beam epitaxy," J Vac Sci Technol A **38**(6), 063406 (2020).
[30] M. Kracht, A. Karg, J. Schörmann, M. Weinhold, D. Zink, F. Michel, M. Rohnke, M. Schowalter, B. Gerken, A. Rosenauer, P.J. Klar, J. Janek, and M. Eickhoff, "Tin-Assisted Synthesis of ε-Ga_2O_3 by Molecular Beam Epitaxy," Phys Rev Appl **8**(5), 1–8 (2017).
[31] J.W. Roberts, P.R. Chalker, B. Ding, R.A. Oliver, J.T. Gibbon, L.A.H. Jones, V.R. Dhanak, L.J. Phillips, J.D. Major, and F.C.-P. Massabuau, "Low temperature growth and optical properties of α-Ga_2O_3 deposited on sapphire by plasma enhanced atomic layer deposition," J Cryst Growth **528**, 125254 (2019).
[32] F. Boschi, M. Bosi, T. Berzina, E. Buffagni, C. Ferrari, and R. Fornari, "Hetero-epitaxy of ε-Ga_2O_3 layers by MOCVD and ALD," J Cryst Growth **443**, 25–30 (2016).
[33] F. Massabuau, J.W. Roberts, D. Nicol, P.R. Edwards, M. McLelland, G.L. Dallas, D.A. Hunter, E.A. Nicolson, J.C. Jarman, A. Kovacs, R.W. Martin, R.A. Oliver, and P.R. Chalker, in *Oxide-Based Materials and Devices XII*, edited by F.H. Teherani, D.C. Look, and D.J. Rogers (SPIE, 2021), p. 20.
[34] T. Oshima, K. Matsuyama, K. Yoshimatsu, and A. Ohtomo, "Conducting Si-doped γ-Ga_2O_3 epitaxial films grown by pulsed-laser deposition," J Cryst Growth **421**, 23–26 (2015).
[35] Y. Cai, K. Zhang, Q. Feng, Y. Zuo, Z. Hu, Z. Feng, H. Zhou, X. Lu, C. Zhang, W. Tang, J. Zhang, and Y. Hao, "Tin-assisted growth of ε-Ga_2O_3 film and the fabrication of photodetectors on sapphire substrate by PLD" Opt Mater Express **8**(11), 3506 (2018).
[36] M. Bosi, P. Mazzolini, L. Seravalli, and R. Fornari, "Ga_2O_3 polymorphs: tailoring the epitaxial growth conditions," J Mater Chem C **8**(32), 10975–10992 (2020).
[37] D. Gogova, G. Wagner, M. Baldini, M. Schmidbauer, K. Irmscher, R. Schewski, Z. Galazka, M. Albrecht, and R. Fornari, "Structural properties of Si-doped β-Ga_2O_3 layers grown by MOVPE," J Cryst Growth **401**, 665–669 (2014).
[38] T. Oshima, T. Nakazono, A. Mukai, and A. Ohtomo, "Epitaxial growth of γ-Ga_2O_3 films by mist chemical vapor deposition," J Cryst Growth **359**, 60–63 (2012).
[39] R. Cuscó, N. Domènech-Amador, T. Hatakeyama, T. Yamaguchi, T. Honda, and L. Artús, "Lattice dynamics of a mist-chemical vapor deposition-grown corundum-like Ga_2O_3 single crystal," J Appl Phys **117**(18), 0–4 (2015).

[40] K. Kaneko, S. Fujita, and T. Hitora, "A power device material of corundum-structured α-Ga_2O_3 fabricated by MIST EPITAXY® technique," Jpn J Appl Phys **57**(2), 6–11 (2018).
[41] H.Y. Kang, H. Kang, E. Lee, G.R. Lee, and R.B.K. Chung, "Sn-Induced Phase Stabilization and Enhanced Thermal Stability of κ-Ga_2O_3 Grown by Mist Chemical Vapor Deposition," ACS Omega **6**(46), 31292–31298 (2021).
[42] D. Tahara, H. Nishinaka, S. Morimoto, and M. Yoshimoto, "Stoichiometric control for heteroepitaxial growth of smooth ε-Ga_2O_3 thin films on *c*-plane AlN templates by mist chemical vapor deposition," Jpn J Appl Phys **56**(7), 078004 (2017).
[43] K. Akaiwa, and S. Fujita, "Electrical conductive corundum-structured α-Ga_2O_3 Thin films on sapphire with tin-doping grown by spray-assisted mist chemical vapor deposition," Jpn J Appl Phys **51**(7 PART 1), (2012).
[44] F. Egyenes-Pörsök, F. Gucmann, K. Hušeková, E. Dobročka, M. Sobota, M. Mikolášek, K. Fröhlich, and M. Tapajna, "Growth of α- And β-Ga_2O_3 epitaxial layers on sapphire substrates using liquid-injection MOCVD," Semicond Sci Tech **35**(11), (2020).
[45] E. Dobročka, F. Gucmann, K. Hušeková, P. Nádaždy, F. Hrubišák, F. Egyenes, A. Rosová, M. Mikolášek, and M. Ťapajna, "Structure and Thermal Stability of ε/κ-Ga_2O_3 Films Deposited by Liquid-Injection MOCVD," Materials **16**(1), (2023).
[46] Z. Feng, M.R. Karim, and H. Zhao, "Low pressure chemical vapor deposition of β-Ga_2O_3 thin films: Dependence on growth parameters," APL Mater **7**(2), 022514 (2019).
[47] Y. Zhang, Z. Feng, M.R. Karim, and H. Zhao, "High-temperature low-pressure chemical vapor deposition of β-Ga_2O_3," J Vac Sci Technol A **38**(5), 050806 (2020).
[48] S. Rafique, M.R. Karim, J.M. Johnson, J. Hwang, and H. Zhao, "LPCVD homoepitaxy of Si doped β-Ga_2O_3 thin films on (010) and (001) substrates," Appl Phys Lett **112**(5), 052104 (2018).
[49] Zhao, H. (2020). Low Pressure Chemical Vapor Deposition. In: Higashiwaki, M., Fujita, S. (eds) Gallium Oxide. Springer Series in Materials Science, vol 293. Springer, Cham. https://doi.org/10.1007/978-3-030-37153-1_16
[50] J. Hu, B. Xu, Z. Zhang, X. He, L. Li, H. Cheng, J. Wang, J. Meng, X. Wang, C. Zhang, R. Jia, and H. Pu, "Step flow growth of β-Ga_2O_3 films on off-axis 4H-SiC substrates by LPCVD," Surf Interfaces **37**, 102732 (2023).
[51] G. Joshi, Y.S. Chauhan, and A. Verma, "Temperature dependence of β-Ga_2O_3 heteroepitaxy on c-plane sapphire using low pressure chemical vapor deposition," J Alloy Compd **883**, 160799 (2021).
[52] P. Mazzolini, A. Falkenstein, C. Wouters, R. Schewski, T. Markurt, Z. Galazka, M. Martin, M. Albrecht, and O. Bierwagen, "Substrate-orientation dependence of β-Ga_2O_3 (100), (010), (001), and ($2\bar{0}1$) homoepitaxy by indium-mediated metal-exchange catalyzed molecular beam epitaxy (MEXCAT-MBE)," APL Mater **8**(1), 011107 (2020).
[53] S.J. Hao, M. Hetzl, F. Schuster, K. Danielewicz, A. Bergmaier, G. Dollinger, Q.L. Sai, C.T. Xia, T. Hoffmann, M. Wiesinger, S. Matich, W. Aigner, and M. Stutzmann, "Growth and characterization of β-Ga_2O_3 thin films on different substrates," J Appl Phys **125**(10), 105701 (2019).
[54] W. Mi, J. Ma, Z. Zhu, C. Luan, Y. Lv, and H. Xiao, "Epitaxial growth of Ga_2O_3 thin films on MgO (110) substrate by metal–organic chemical vapor deposition," J Cryst Growth **354**(1), 93–97 (2012).

[55] H. Nishinaka, D. Tahara, and M. Yoshimoto, "Heteroepitaxial growth of ε-Ga_2O_3 thin films on cubic (111) MgO and (111) yttria-stablized zirconia substrates by mist chemical vapor deposition," Jpn J Appl Phys **55**(12), 1202BC (2016).
[56] G. Pozina, C.-W. Hsu, N. Abrikossova, M.A. Kaliteevski, and C. Hemmingsson, "Development of β-Ga_2O_3 layers growth on sapphire substrates employing modeling of precursors ratio in halide vapor phase epitaxy reactor," Sci Rep **10**(1), 22261 (2020).
[57] D. Gogova, M. Ghezellou, D.Q. Tran, S. Richter, A. Papamichail, J. ul Hassan, A.R. Persson, P.O.Å. Persson, O. Kordina, B. Monemar, M. Hilfiker, M. Schubert, P.P. Paskov, and V. Darakchieva, "Epitaxial growth of *β*-Ga_2O_3 by hot-wall MOCVD," AIP Adv **12**(5), 055022 (2022).
[58] T. Hadamek, A.B. Posadas, F. Al-Quaiti, D.J. Smith, M.R. McCartney, and A.A. Demkov, "β-Ga_2O_3 on Si (001) grown by plasma-assisted MBE with γ-Al_2O_3 (111) buffer layer: Structural characterization," AIP Adv **11**(4), 045209 (2021).
[59] Y. Berencén, Y. Xie, M. Wang, S. Prucnal, L. Rebohle, and S. Zhou, "Structural and optical properties of pulsed-laser deposited crystalline *β*-Ga_2O_3 thin films on silicon," Semicond Sci Tech **34**(3), 035001 (2019).
[60] K. Gu, Z. Zhang, K. Tang, J. Huang, Y. Shang, Y. Shen, M. Liao, and L. Wang, "Effect of a seed layer on microstructure and electrical properties of Ga_2O_3 films on variously oriented Si substrates," Vacuum **195**, 110671 (2022).
[61] R. Saha, S. Sikdar, B.N. Chowdhury, A. Karmakar, and S. Chattopadhyay, "Catalyst-modified vapor-liquid-solid (VLS) growth of single crystalline β-Gallium Oxide (Ga_2O_3) thin film on Si-substrate," Superlattice Microst **136**, 106316 (2019).
[62] A.J. Green, J. Speck, G. Xing, P. Moens, F. Allerstam, K. Gumaelius, T. Neyer, A. Arias-Purdue, V. Mehrotra, A. Kuramata, K. Sasaki, S. Watanabe, K. Koshi, J. Blevins, O. Bierwagen, S. Krishnamoorthy, K. Leedy, A.R. Arehart, A.T. Neal, S. Mou, S.A. Ringel, A. Kumar, A. Sharma, K. Ghosh, U. Singisetti, W. Li, K. Chabak, K. Liddy, A. Islam, S. Rajan, S. Graham, S. Choi, Z. Cheng, and M. Higashiwaki, "β-Gallium oxide power electronics," APL Mater **10**(2), 029201 (2022).
[63] B. Chatterjee, K. Zeng, C.D. Nordquist, U. Singisetti, and S. Choi, "Device-Level Thermal Management of Gallium Oxide Field-Effect Transistors," IEEE T Comp Pack Man **9**(12), 2352–2365 (2019).
[64] T. Matsumae, Y. Kurashima, H. Umezawa, K. Tanaka, T. Ito, H. Watanabe, and H. Takagi, "Low-temperature direct bonding of β-Ga_2O_3 and diamond substrates under atmospheric conditions," Appl Phys Lett **116**(14), 141602 (2020).
[65] Y. Xu, F. Mu, Y. Wang, D. Chen, X. Ou, and T. Suga, "Direct wafer bonding of Ga_2O_3–SiC at room temperature," Ceram Int **45**(5), 6552–6555 (2019).
[66] Z. Shen, W. Xu, Y. Chen, J. Lin, Y. Xie, K. Huang, T. You, G. Han, and X. Ou, "Wafer-scale single-crystalline β-Ga_2O_3 thin film on SiC substrate by ion-cutting technique with hydrophilic wafer bonding at elevated temperatures," Sci China Mater **66**(2), 756–763 (2023).
[67] W. Chen, Z. Chen, Z. Li, Z. Fei, Y. Pei, G. Wang, and Z. He, "Heteroepitaxy of ε-Ga_2O_3 thin films grown on AlN/Si(1 1 1) templates by metal–organic chemical vapor deposition," Appl Surf Sci **581**, 152335 (2022).
[68] Z. Cheng, V.D. Wheeler, T. Bai, J. Shi, M.J. Tadjer, T. Feygelson, K.D. Hobart, M.S. Goorsky, and S. Graham, "Integration of polycrystalline Ga_2O_3 on diamond for thermal management," Appl Phys Lett **116**(6), 062105 (2020).

[69] S. Mandal, K. Arts, H.C.M. Knoops, J.A. Cuenca, G.M. Klemencic, and O.A. Williams, "Surface zeta potential and diamond growth on gallium oxide single crystal," Carbon N Y **181**, 79–86 (2021).
[70] M. Malakoutian, Y. Song, C. Yuan, C. Ren, J.S. Lundh, R.M. Lavelle, J.E. Brown, D.W. Snyder, S. Graham, S. Choi, and S. Chowdhury, "Polycrystalline diamond growth on β-Ga_2O_3 for thermal management," Appl Phys Express **14**(5), 055502 (2021).
[71] M.R. Karim, Z. Chen, Z. Feng, H.-L. Huang, J.M. Johnson, M.J. Tadjer, J. Hwang, and H. Zhao, "Two-step growth of β-Ga_2O_3 films on (100) diamond via low pressure chemical vapor deposition," J Vac Sci Technol A **39**(2), 023411 (2021).
[72] C. Yuan, J. Li, L. Lindsay, D. Cherns, J.W. Pomeroy, S. Liu, J.H. Edgar, and M. Kuball, "Modulating the thermal conductivity in hexagonal boron nitride via controlled boron isotope concentration," Commun Phys **2**(1), 1–8 (2019).
[73] Y. Zhou, R. Ramaneti, J. Anaya, S. Korneychuk, J. Derluyn, H. Sun, J. Pomeroy, J. Verbeeck, K. Haenen, and M. Kuball, "Thermal characterization of polycrystalline diamond thin film heat spreaders grown on GaN HEMTs," Appl Phys Lett **111**(4), 041901 (2017).
[74] P. Šichman, S. Hasenöhrl, R. Stoklas, J. Priesol, E. Dobročka, Š. Haščík, F. Gucmann, A. Vincze, A. Chvála, J. Marek, A. Šatka, and J. Kuzmik, "Semi-insulating GaN for vertical structures: role of substrate selection and growth pressure," Mat Sci Semicon Proc **118**, 105203 (2020).
[75] S. Nakagomi, and Y. Kokubun, "Crystal orientation of β-Ga_2O_3 thin films formed on c-plane and a-plane sapphire substrate," J Cryst Growth **349**(1), 12–18 (2012).
[76] W. Xu, J. Shi, Y. Li, X. Xiu, S. Ding, Z. Xie, T. Tao, P. Chen, B. Liu, R. Zhang, and Y. Zheng, "Study of β-Ga_2O_3 films hetero-epitaxially grown on off-angled sapphire substrates by halide vapor phase epitaxy," Mater Lett **289**, 129411 (2021).
[77] S.-H. Cho, Y.-J. Shin, S.-M. Jeong, S.-H. Kwon, and S.-Y. Bae, "Two-step growth of κ-Ga_2O_3 thin films on 4H-SiC substrates with temperature-varied buffer layers using mist chemical vapor deposition," Jpn J Appl Phys **62**(1), 015508 (2023).
[78] H. Nishinaka, O. Ueda, Y. Ito, N. Ikenaga, N. Hasuike, and M. Yoshimoto, "Plan-view TEM observation of a single-domain κ-Ga_2O_3 thin film grown on ε-$GaFeO_3$ substrate using $GaCl_3$ precursor by mist chemical vapor deposition," Jpn J Appl Phys **61**(1), 018002 (2022).
[79] F. Zhang, X. Liu, J. Zhou, Q. Liao, T. Sun, X. Liu, Y. Peng, D. Guo, P. Wang, and H. Li, "The spontaneous polarization of In-doped κ-Ga_2O_3 by first-principles calculation," AIP Adv **12**(10), 105115 (2022).
[80] Y. Kuang, X. Chen, T. Ma, Q. Du, Y. Zhang, J. Hao, F.-F. Ren, B. Liu, S. Zhu, S. Gu, R. Zhang, Y. Zheng, and J. Ye, "Band Alignment and Enhanced Interfacial Conductivity Manipulated by Polarization in a Surfactant-Mediated Grown κ-Ga_2O_3/In_2O_3 Heterostructure," ACS Appl Electron Mater **3**(2), 795–803 (2021).
[81] H.Y. Kang, M.J. Yeom, J.Y. Yang, Y. Choi, J. Lee, C. Park, G. Yoo, and R.B. Kyu Chung, "Epitaxial κ-Ga_2O_3/GaN heterostructure for high electron-mobility transistors," Mater Today Phys **31**, 101002 (2023).
[82] Y. Song, P. Ranga, Y. Zhang, Z. Feng, H.-L. Huang, M.D. Santia, S.C. Badescu, C.U. Gonzalez-Valle, C. Perez, K. Ferri, R.M. Lavelle, D.W. Snyder, B.A. Klein, J. Deitz, A.G. Baca, J.-P. Maria, B. Ramos-Alvarado, J. Hwang, H. Zhao, X. Wang, S. Krishnamoorthy, B.M. Foley, and S. Choi, "Thermal Conductivity of β-Phase Ga_2O_3 and

$(Al_xGa_{1-x})_2O_3$ Heteroepitaxial Thin Films," ACS Appl Mater Interfaces **13**(32), 38477–38490 (2021).
[83] Z. Cheng, F. Mu, T. You, W. Xu, J. Shi, M.E. Liao, Y. Wang, K. Huynh, T. Suga, M.S. Goorsky, X. Ou, and S. Graham, "Thermal Transport across Ion-Cut Monocrystalline β-Ga_2O_3 Thin Films and Bonded β-Ga_2O_3–SiC Interfaces," ACS Appl Mater Interfaces **12**(40), 44943–44951 (2020).
[84] R. Wei, S. Song, K. Yang, Y. Cui, Y. Peng, X. Chen, X. Hu, and X. Xu, "Thermal conductivity of 4H-SiC single crystals," J Appl Phys **113**(5), 053503 (2013).
[85] M. Slomski, N. Blumenschein, P.P. Paskov, J.F. Muth, and T. Paskova, "Anisotropic thermal conductivity of β-Ga_2O_3 at elevated temperatures: Effect of Sn and Fe dopants," J Appl Phys **121**(23), 235104 (2017).
[86] F. Hrubisak, K. Husekova, F. Egyenes, A. Rosova, A. Kubranska, E. Dobrocka, P. Nadazdy, J. Keshtkar, F. Gucmann, and M. Tapajna, in *2022 14th International Conference on Advanced Semiconductor Devices and Microsystems (ASDAM)* (IEEE, 2022), pp. 1–4.
[87] S. García, I. Íñiguez-de-la-Torre, J. Mateos, T. González, and S. Pérez, "Impact of substrate and thermal boundary resistance on the performance of AlGaN/GaN HEMTs analyzed by means of electro-thermal Monte Carlo simulations," Semicond Sci Tech **31**(6), 065005 (2016).

Tables

TABLE I. Summary of used Ga_2O_3 growth parameters.

Sample	Ga_2O_3 phase	Precursor	Growth temperature (°C)	O_2/Ar flow (sccm)	Pressure (Torr)	Growth rate (nm/h)	Thickness (nm)
A	β	$Ga(acac)_3$	700	600/120	1.68	63	88
B	β	$Ga(thd)_3$	700	600/120	1.68	40	55
C	κ	$Ga(thd)_3$	600	800/120	2.06	27	35

Figure captions

FIG. 1. Schematics of used LI-MOCVD setup used for Ga_2O_3 growth and prepared thin films.

FIG. 2. XPS results for β-Ga_2O_3 (sample A). Surface XPS survey spectrum; only Ga, O, and C signals were observed (a) and calculated depth-resolved atomic percentages of Ga, O, and C after Ar^+ ion sputtering (b). Etch time at 0 s corresponds to the sample surface.

FIG. 3. Symmetric ω/2θ XRD scans of sample A and B – β-Ga_2O_3 (a) and sample C – κ-Ga_2O_3 (b). Inset in (b) shows detail of the 006 κ-Ga_2O_3-related diffraction with a shoulder attributed to $\bar{6}03$ diffraction of the parasitic β-Ga_2O_3.

FIG. 4. XRD φ scans of prepared β- and κ-Ga_2O_3 films. Sample A showing six maxima related to 002 and 400 diffractions of β-Ga_2O_3 and related 103 diffraction of 4H-SiC substrate (a). Sample C showing six maxima related to 016 diffraction of κ-Ga_2O_3, 002 and 400 diffractions of parasitic β-Ga_2O_3 contribution (right intensity scale), and 103 diffraction of 4H-SiC substrate (left intensity scale) (b).

FIG. 5. A map showing the influence of growth temperature and O_2 flow on the inclusion of parasitic β-Ga_2O_3 phase in κ-Ga_2O_3 films grown by LI-MOCVD on 4H-SiC. Z-scale represents the ratio of κ to β peak heights determined by Gaussian fitting of ω/2θ XRD diffractions at the locations of $\bar{6}03$ and 006 diffractions of β and κ-Ga_2O_3, respectively.

FIG. 6. SEM image of the surface of sample A (a). Schematic representation of epitaxial relation between the β-Ga_2O_3 layer (red, yellow, and green rectangles) and 4H-SiC substrate (black triangles) (b). TEM plan view of sample A (c) and corresponding indexed SAED pattern (d). The white indices correspond to the SiC substrate and colored ones correspond to different domain orientations of β-Ga_2O_3. Colors used correspond to those used the schematic showed in (b).

FIG. 7. TEM plan view of sample C (a) with corresponding SAED pattern (b). Schematic representation of epitaxial relation between the κ-Ga_2O_3 domain orientations (red, yellow, and green rectangles) and 4H-SiC substrate (black triangles) (c). Detail SAED pattern corresponding to the area in (b) denoted by white rectangle (d).

FIG. 8. Cross-sectional TEM of κ-Ga_2O_3 (sample C). Bright field (a) and dark field TEM images (b) and corresponding SAED pattern (c). White indices in (c) correspond to 4H-SiC substrate and the cyan indices correspond to different κ-Ga_2O_3 domain orientations. The DF image in (b) was taken using 013 diffraction.

FIG. 9. AFM-resolved surface morphology. β-Ga_2O_3 grown using $Ga(acac)_3$ – sample A (a) and $Ga(thd)_3$ – sample B precursors. κ-Ga_2O_3 grown using $Ga(thd)_3$ precursor – sample C. Also shown are corresponding line profiles taken along dashed lines. Following respective RMS surface roughness for samples A, B, and C were determined: 6.5 nm, 6.8 nm, and 0.9 nm.

FIG. 10. TTR signals and 3-layers model fitting results for β-Ga_2O_3 (a) and κ-Ga_2O_3 (b).

FIG. 11. TTR sensitivity analysis for β-Ga_2O_3 (a) and κ-Ga_2O_3 (b).

FIG. 12. Simulated device depth temperature profiles for various thicknesses of the Ga_2O_3 layer at 3 W/mm. Temperatures for homoepitaxial Ga_2O_3 device are shown for comparison.

Journal of Vacuum Science & Technology A

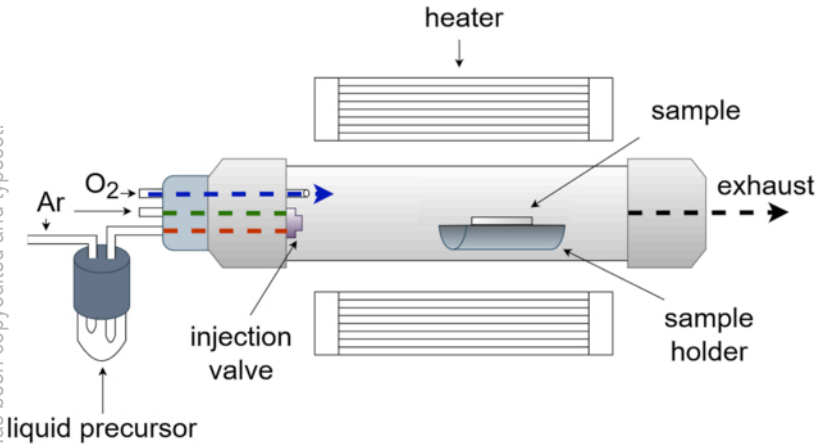

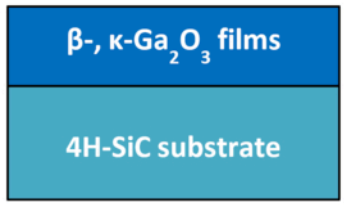

Journal of Vacuum
Science & Technology A

Journal of Vacuum Science & Technology A

ACCEPTED MANUSCRIPT

PLEASE CITE THIS ARTICLE AS DOI: 10.1116/6.0002649

Journal of Vacuum Science & Technology A

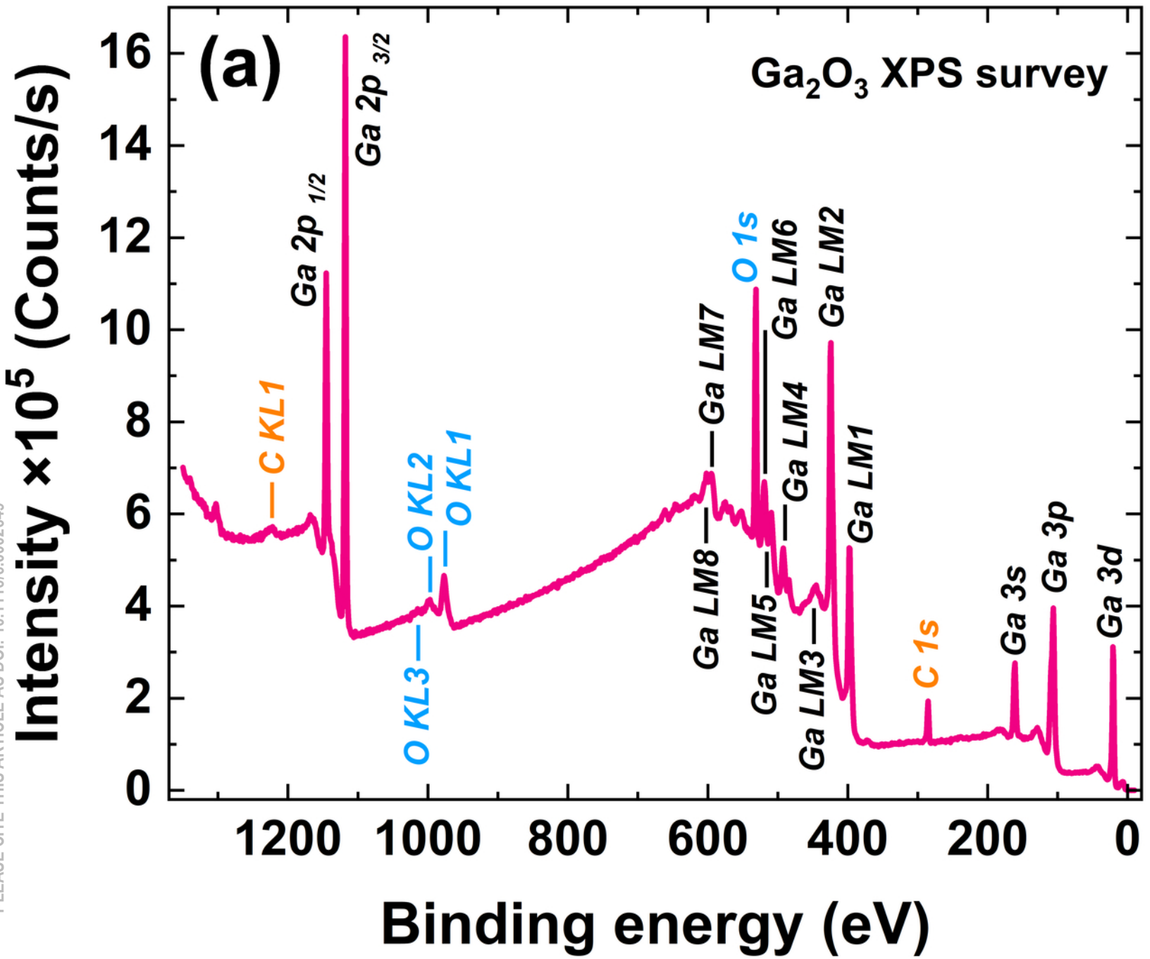

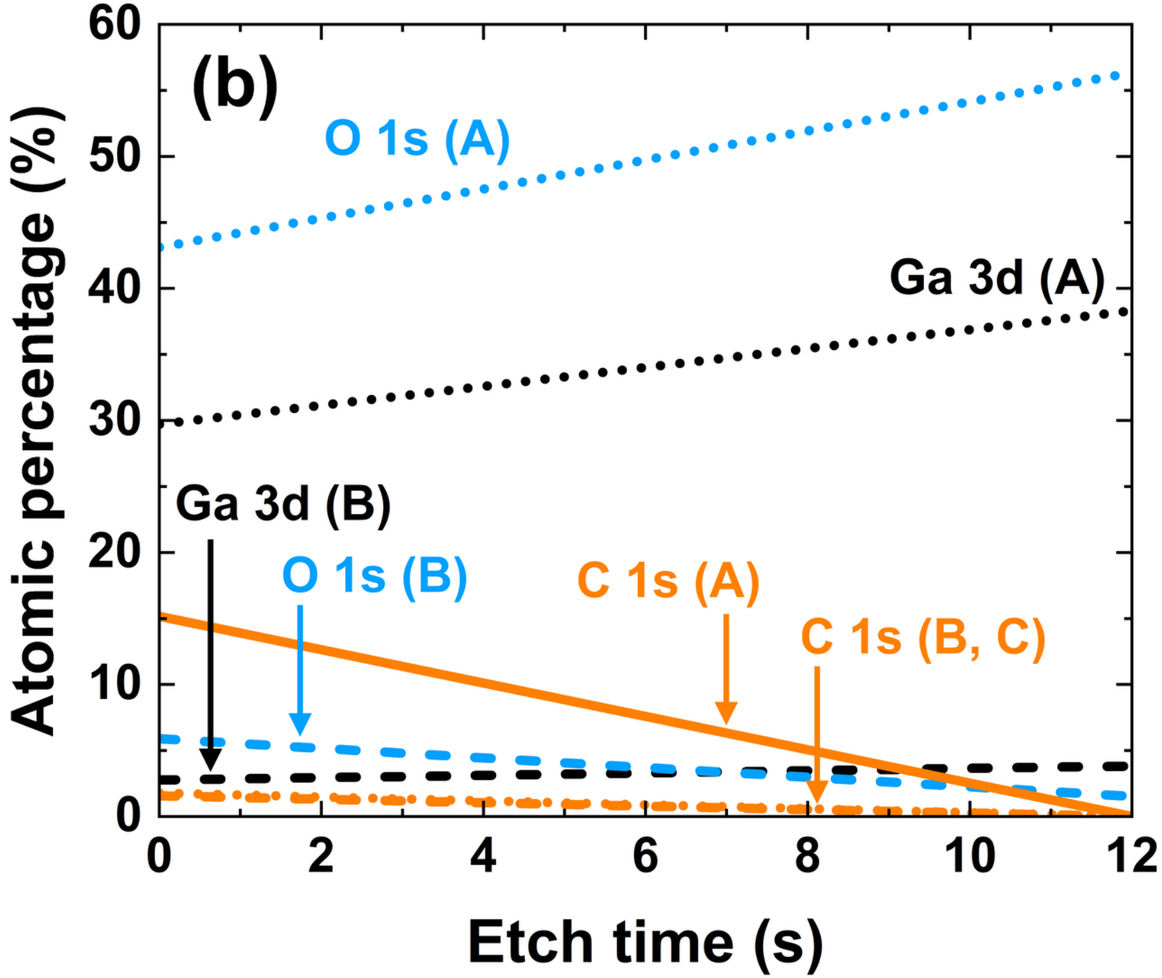

Journal of Vacuum Science & Technology A

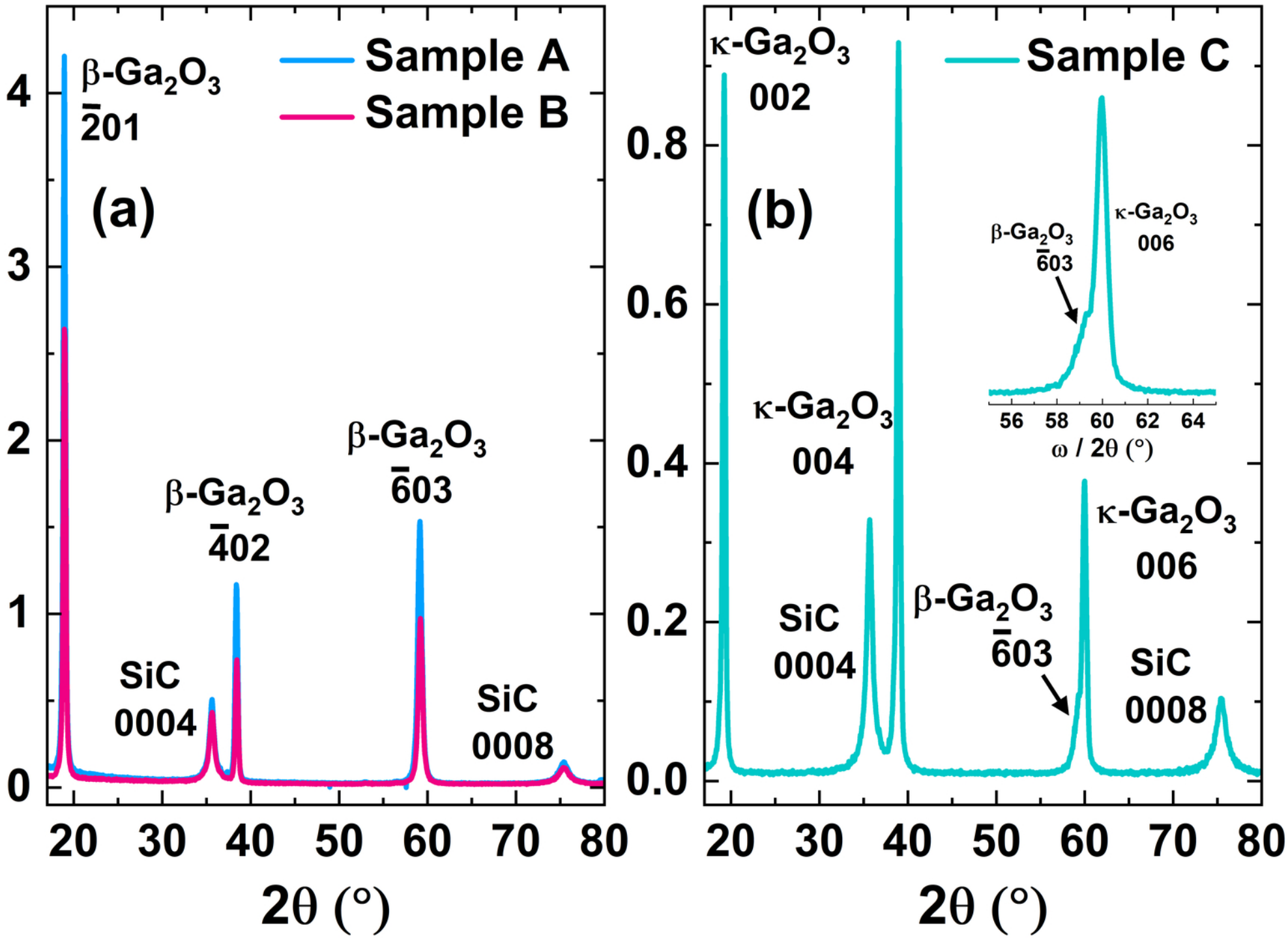

Journal of Vacuum Science & Technology A

PLEASE CITE THIS ARTICLE AS DOI: 10.1116/6.0002649

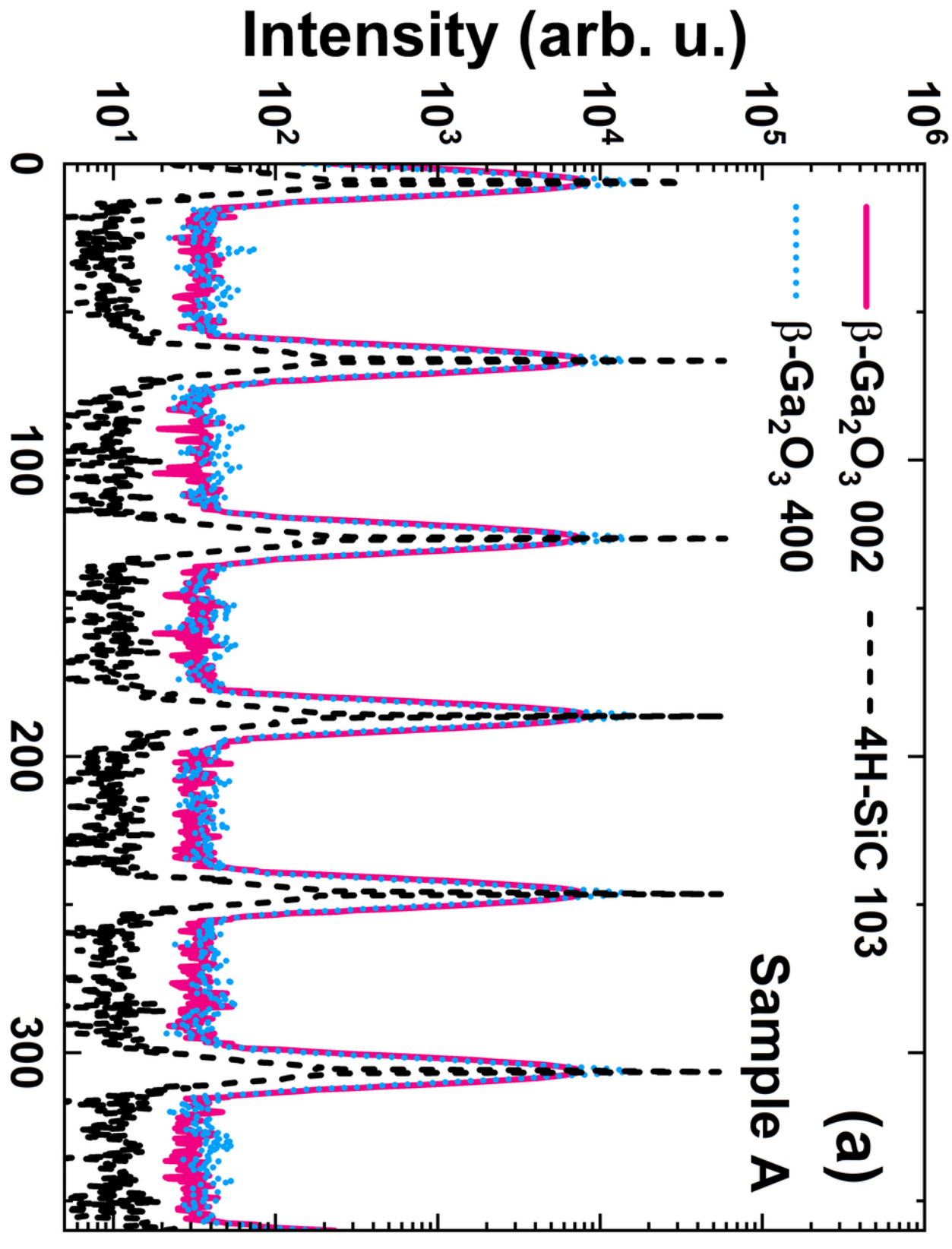

Journal of Vacuum Science & Technology A

ACCEPTED MANUSCRIPT

This is the author's peer reviewed, accepted manuscript. However, the online version of record will be different from this version once it has been copyedited and typeset.
PLEASE CITE THIS ARTICLE AS DOI: 10.1116/6.0002649

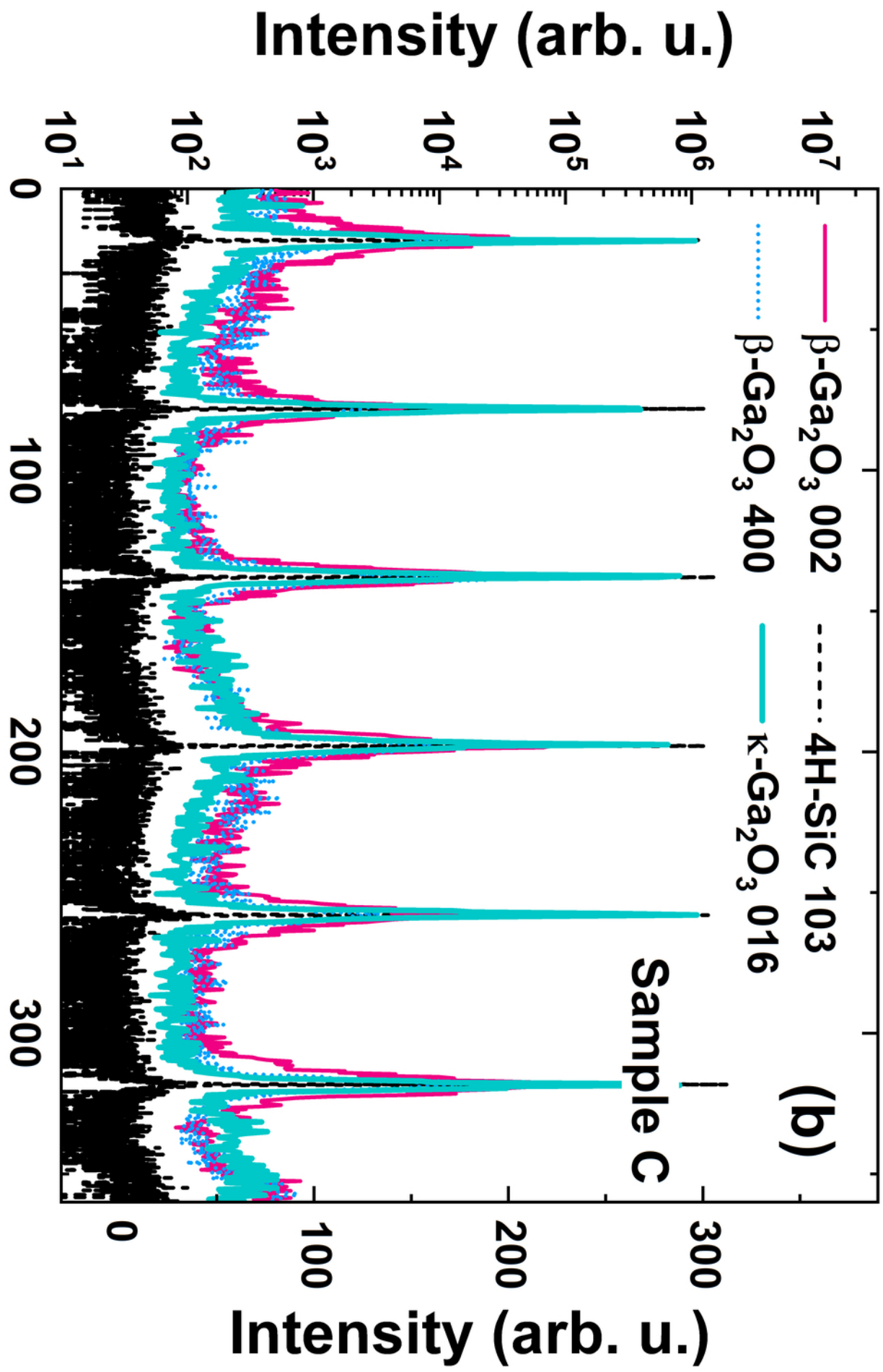

Journal of Vacuum Science & Technology A

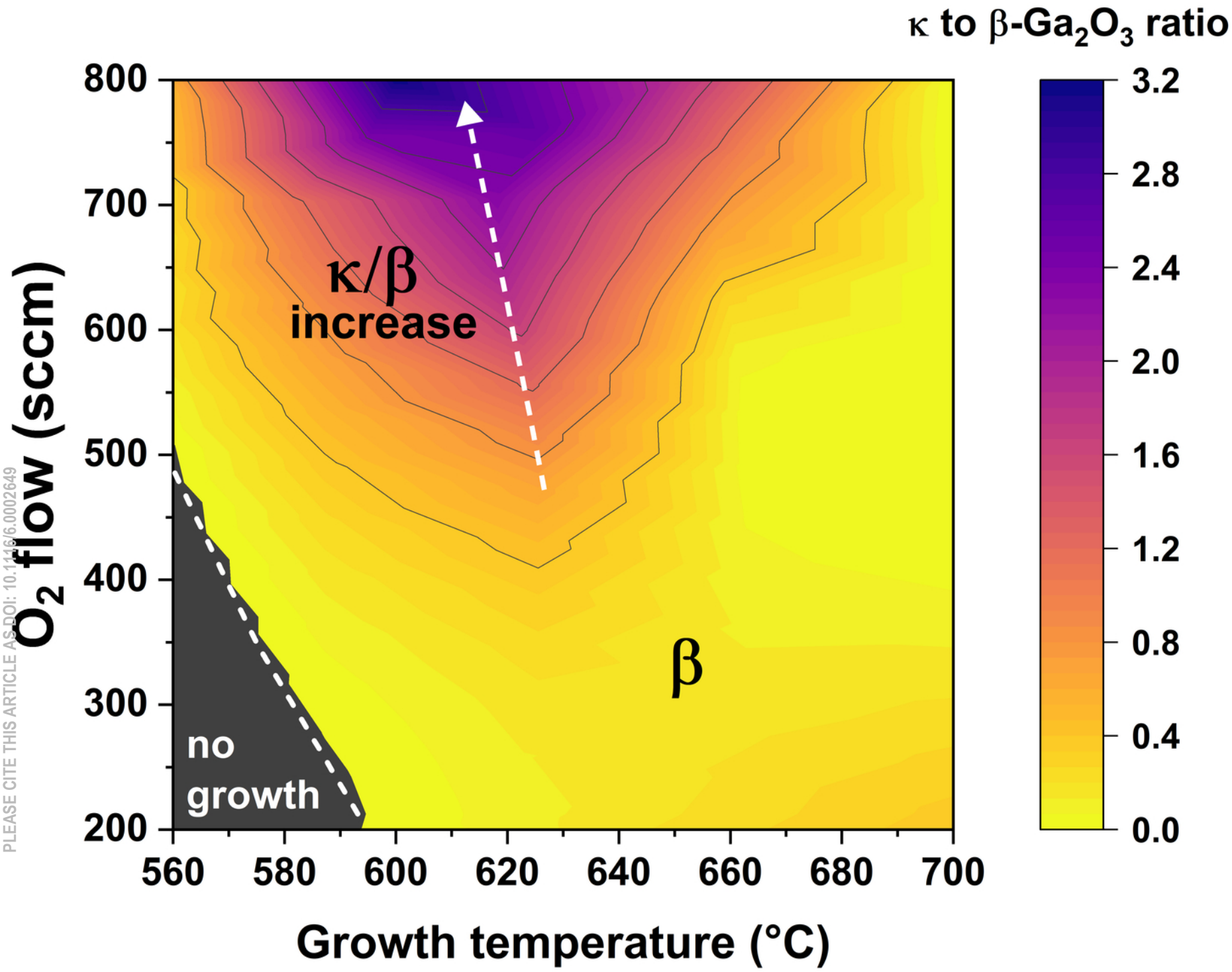

Journal of Vacuum Science & Technology A

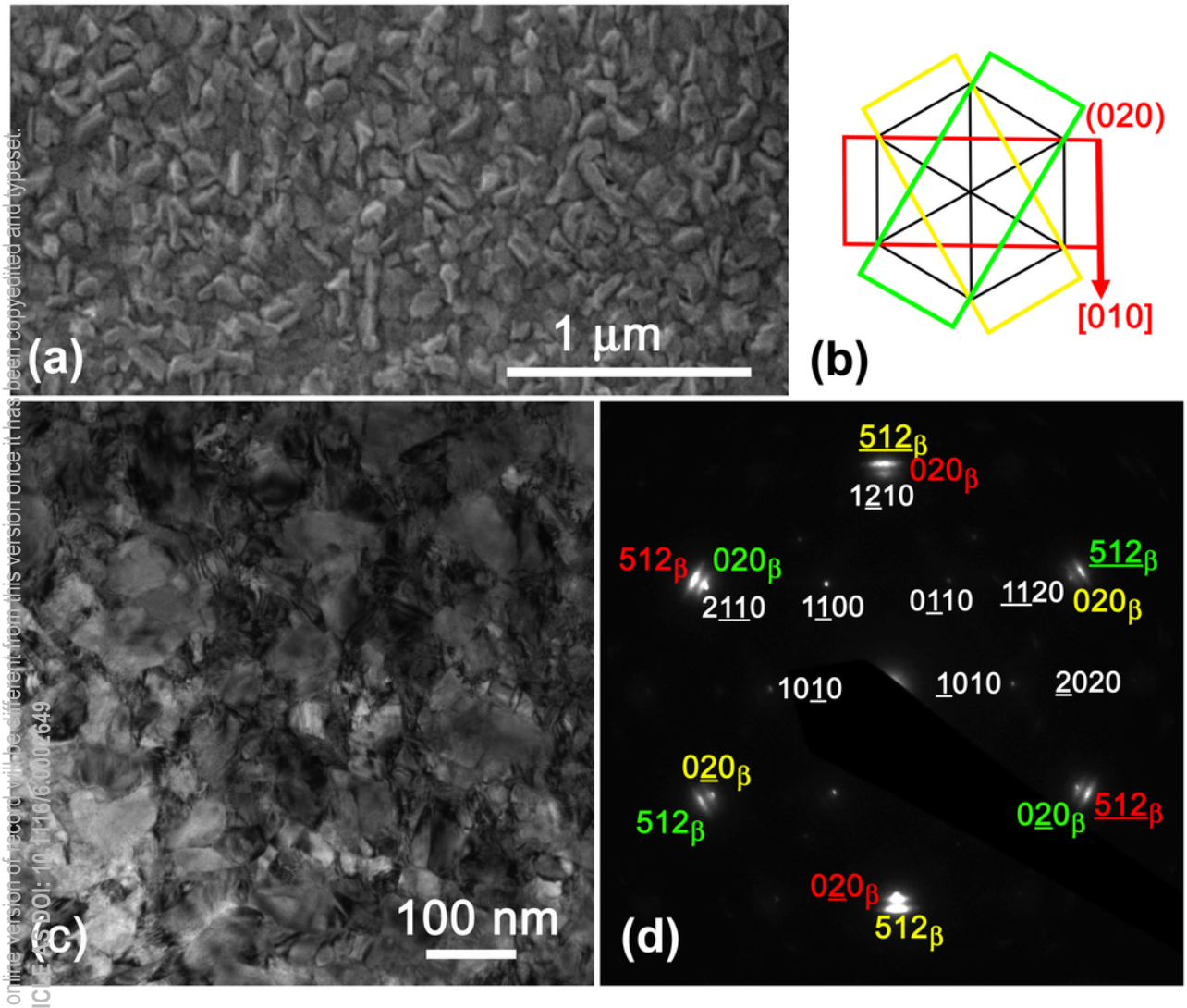

Journal of Vacuum Science & Technology A

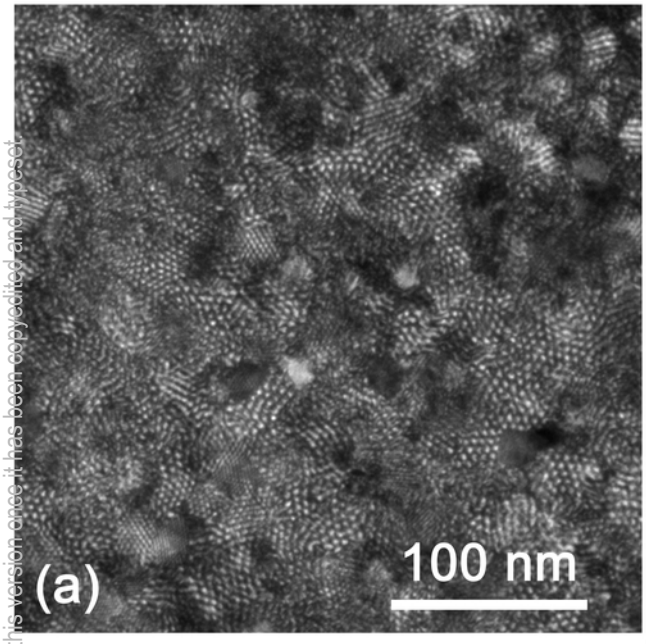

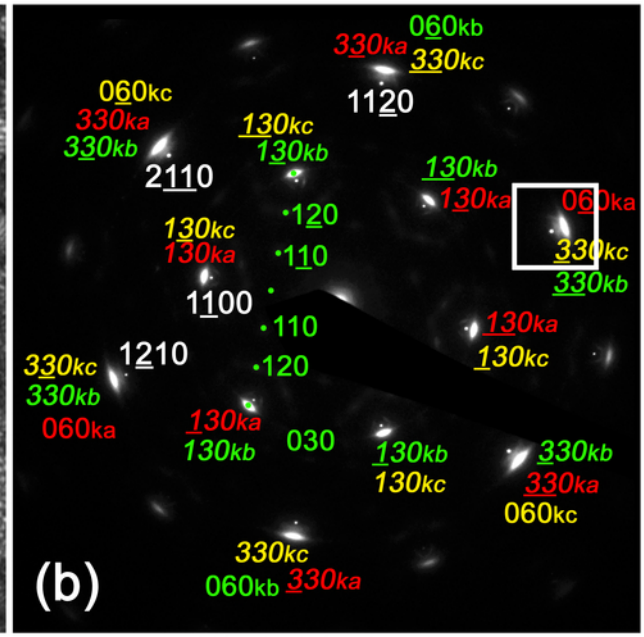

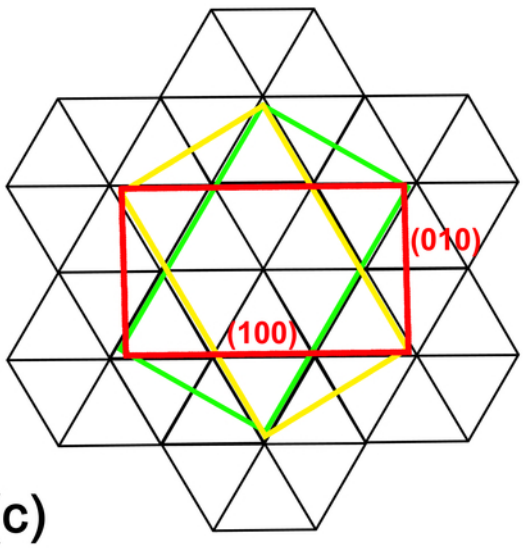

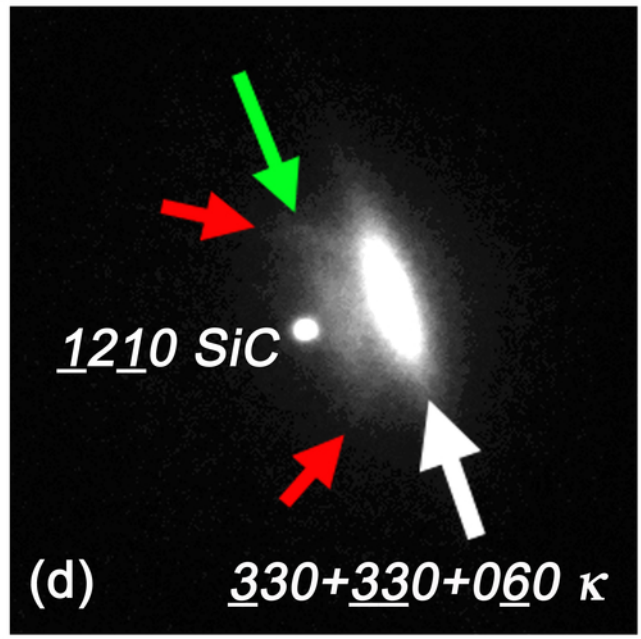

Journal of Vacuum Science & Technology A

PLEASE CITE THIS ARTICLE AS DOI: 10.1116/6.0002649

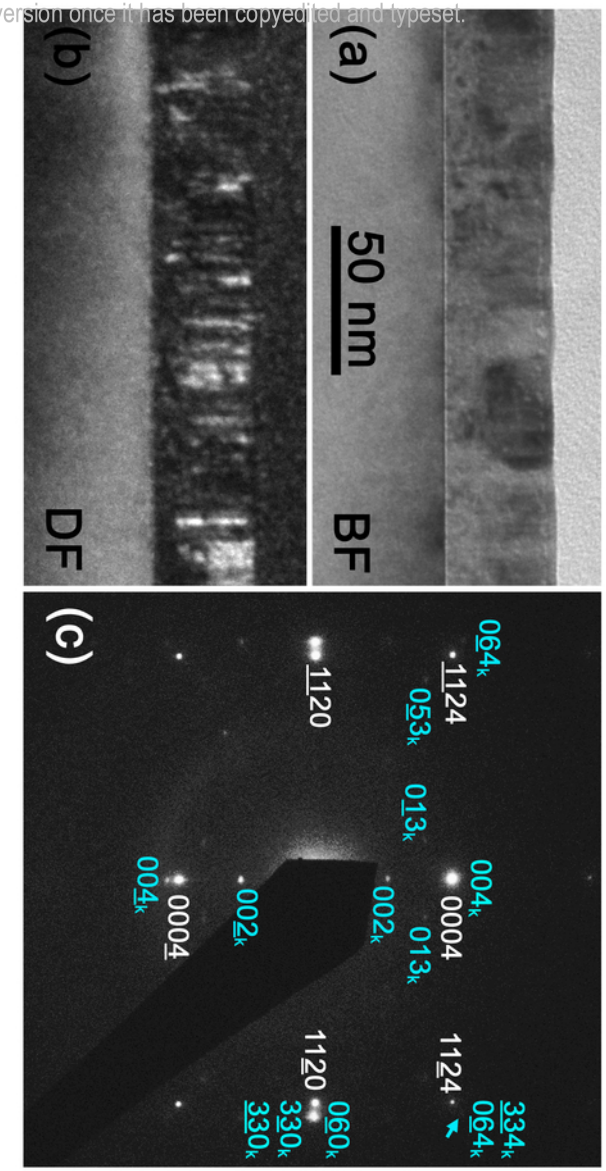

Journal of Vacuum Science & Technology A

PLEASE CITE THIS ARTICLE AS DOI: 10.1116/6.0002649

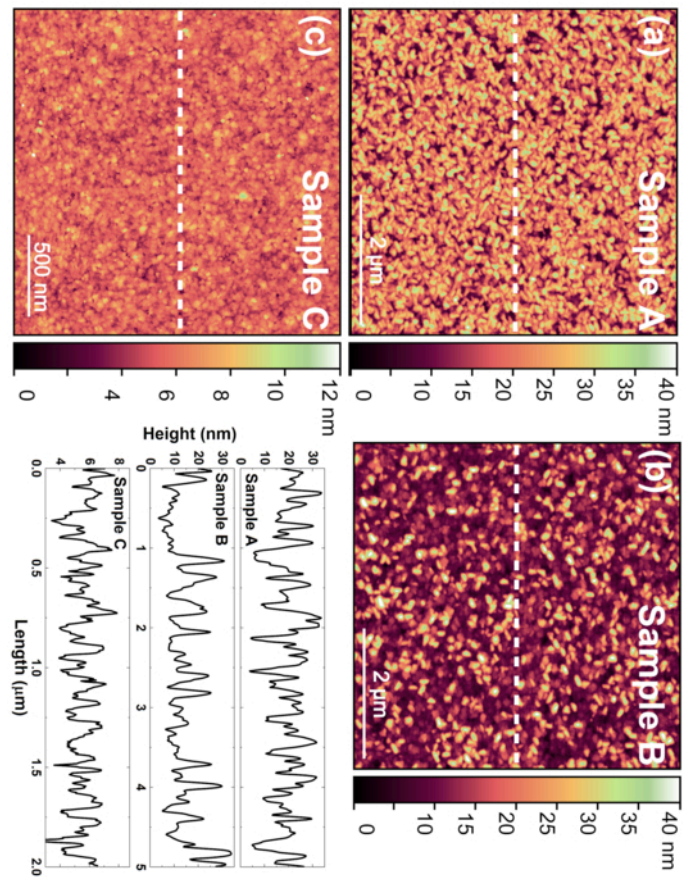

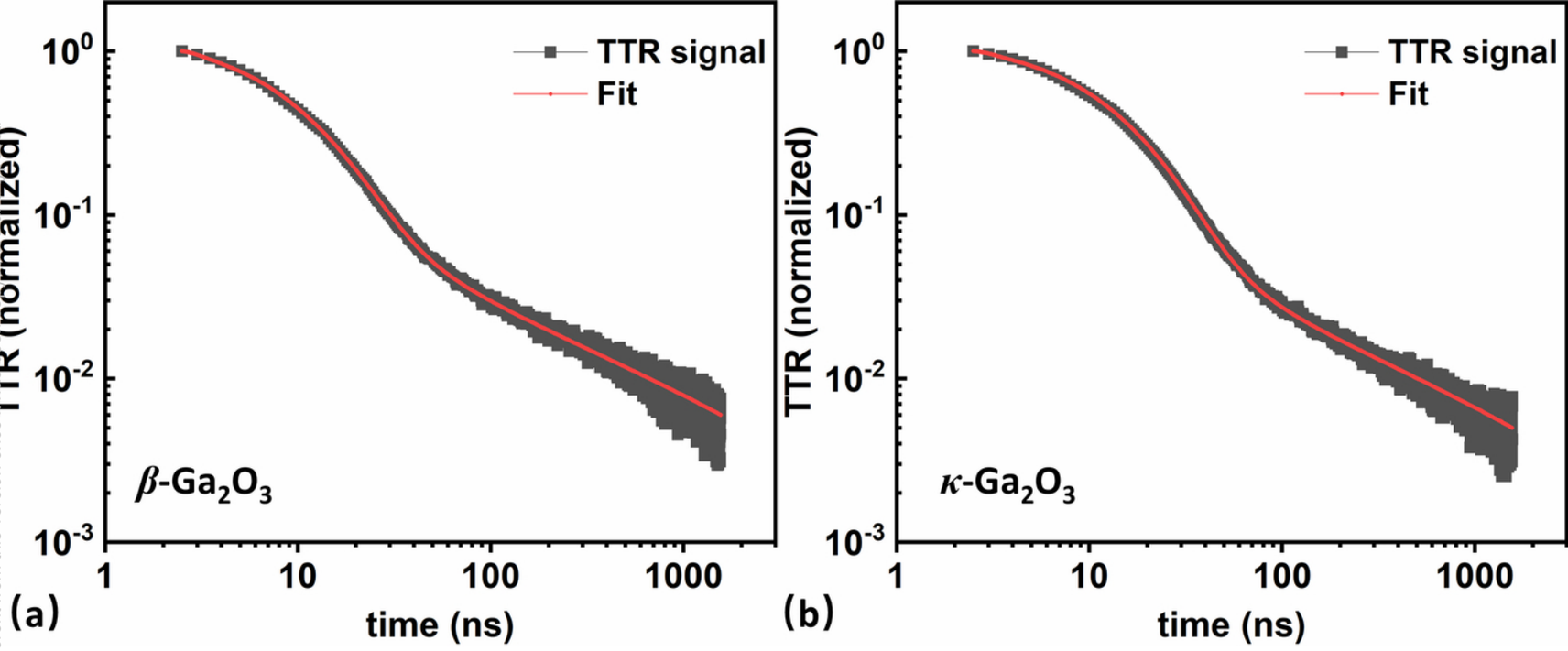

Journal of Vacuum Science & Technology A

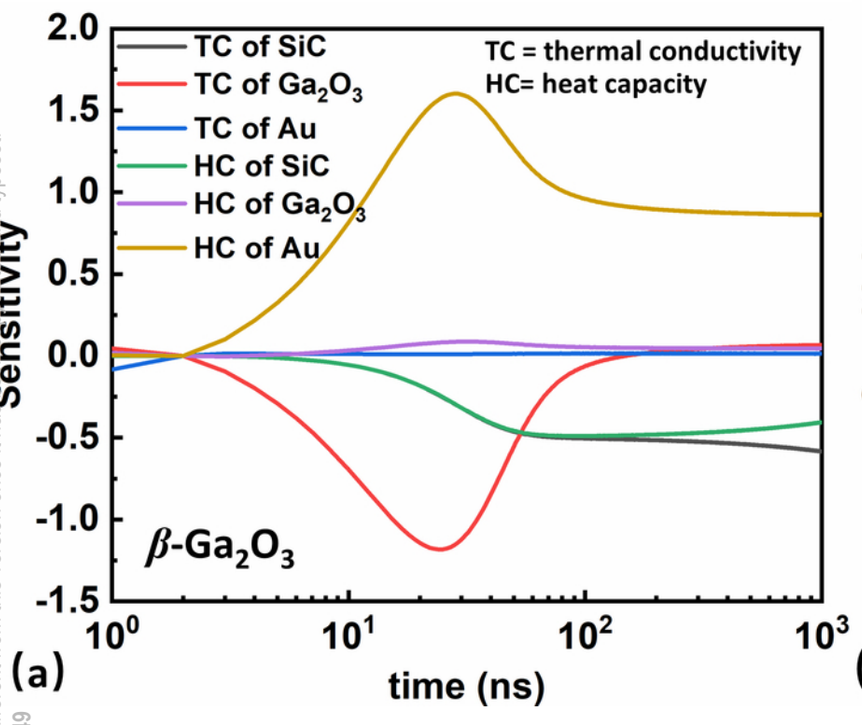

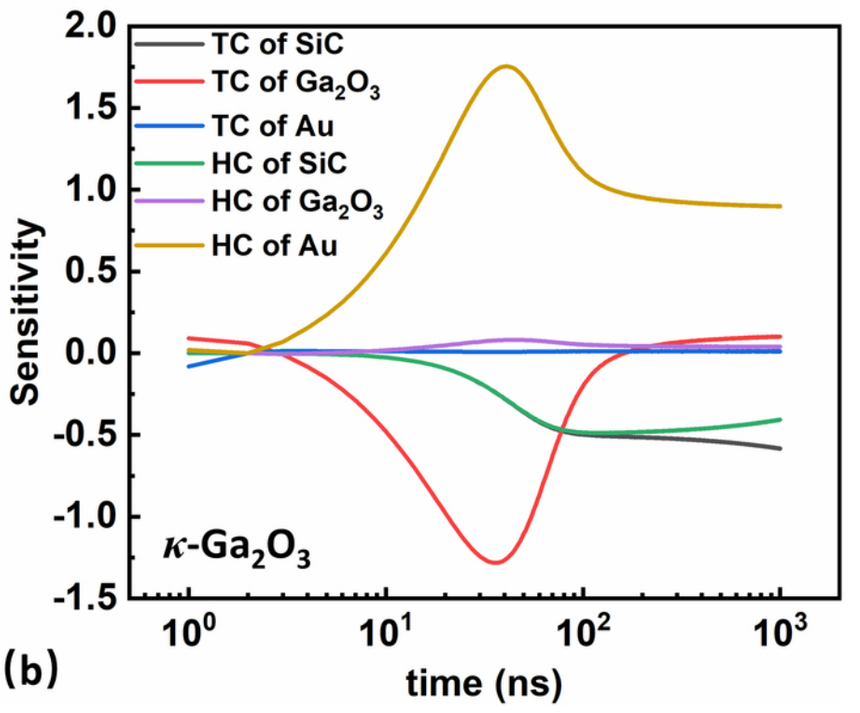

Journal of Vacuum Science & Technology A